



This is a repository copy of *The Causes of Quasi-homologous CMEs*.

White Rose Research Online URL for this paper:
<http://eprints.whiterose.ac.uk/121189/>

Version: Published Version

Article:

Liu, L., Wang, Y., Liu, R. et al. (8 more authors) (2017) The Causes of Quasi-homologous CMEs. *Astrophysical Journal*, 844 (2). 141. ISSN 0004-637X

<https://doi.org/10.3847/1538-4357/aa7d56>

Reuse

Unless indicated otherwise, fulltext items are protected by copyright with all rights reserved. The copyright exception in section 29 of the Copyright, Designs and Patents Act 1988 allows the making of a single copy solely for the purpose of non-commercial research or private study within the limits of fair dealing. The publisher or other rights-holder may allow further reproduction and re-use of this version - refer to the White Rose Research Online record for this item. Where records identify the publisher as the copyright holder, users can verify any specific terms of use on the publisher's website.

Takedown









If you consider content in White Rose Research Online to be in breach of UK law, please notify us by emailing eprints@whiterose.ac.uk including the URL of the record and the reason for the withdrawal request.



eprints@whiterose.ac.uk
<https://eprints.whiterose.ac.uk/>



The Causes of Quasi-homologous CMEs

Lijuan Liu^{1,2,3}, Yuming Wang^{1,4} , Rui Liu^{1,3} , Zhenjun Zhou^{1,5}, M. Temmer⁶ , J. K. Thalmann⁶ ,
Jiajia Liu^{1,4} , Kai Liu^{1,4} , Chenglong Shen^{1,4}, Quanhao Zhang^{1,5} , and A. M. Veronig⁶ 

¹ CAS Key Laboratory of Geospace Environment, Department of Geophysics and Planetary Sciences, University of Science and Technology of China, Hefei, Anhui, 230026, China; ymwang@ustc.edu.cn, ljlju@mail.ustc.edu.cn

² School of Atmospheric Sciences, Sun Yat-sen University, Zhuhai, Guangdong, 519000, China

³ Collaborative Innovation Center of Astronautical Science and Technology, China

⁴ Synergetic Innovation Center of Quantum Information & Quantum Physics, University of Science and Technology of China, Hefei, Anhui 230026, China

⁵ Mengcheng National Geophysical Observatory, University of Science and Technology of China, China

⁶ Institute of Physics/IGAM, University of Graz, Universitätsplatz 5/II, A-8010 Graz, Austria

Received 2017 January 24; revised 2017 June 25; accepted 2017 June 27; published 2017 August 1

Abstract

In this paper, we identified the magnetic source locations of 142 quasi-homologous (QH) coronal mass ejections (CMEs), of which 121 are from solar cycle (SC) 23 and 21 from SC 24. Among those CMEs, 63% originated from the same source location as their predecessor (defined as S-type), while 37% originated from a different location within the same active region as their predecessor (defined as D-type). Their distinctly different waiting time distributions, peaking around 7.5 and 1.5 hr for S- and D-type CMEs, suggest that they might involve different physical mechanisms with different characteristic timescales. Through detailed analysis based on nonlinear force-free coronal magnetic field modeling of two exemplary cases, we propose that the S-type QH CMEs might involve a recurring energy release process from the same source location (by magnetic free energy replenishment), whereas the D-type QH CMEs can happen when a flux tube system is disturbed by a nearby CME.

Key words: Sun: activity – Sun: corona – Sun: coronal mass ejections (CMEs) – Sun: flares – Sun: magnetic fields

Supporting material: animations

1. Introduction

Coronal mass ejections (CMEs), huge expulsions of plasma and magnetic fields from the solar corona, are among the drivers of hazardous space weather. Besides the knowledge on the propagation of a CME in interplanetary space, a successful space weather forecast also requires a precise understanding of the physical mechanisms behind CMEs, as well as their relation to other phenomena in the solar atmosphere. CMEs may originate from either active regions (ARs) or quiescent filament regions (e.g., Schmieder 2006; Webb & Howard 2012). Statistical studies suggest that about two-thirds of CMEs originate from ARs, although the percentages vary from 63% to 85% in different studied samples (Subramanian & Dere 2001; Zhou et al. 2003; Chen et al. 2011). The flare and CME productivity of different ARs varies (e.g., Tian et al. 2002; Akiyama et al. 2007; Chen et al. 2011; Liu et al. 2016a). Some ARs barely produce an eruption, some produce numerous subsequent flares without accompanying CME (e.g., Sun et al. 2015; Thalmann et al. 2015; Liu et al. 2016a), and some others can generate many flare-associated CMEs within a short duration. It appears that ARs that accumulate large amounts of magnetic free energy tend to produce a larger number of and more powerful flares and CMEs than ARs with a small magnetic free energy budget (e.g., Jing et al. 2010; Su et al. 2014). Additionally, the larger a flare, the more likely it is accompanied by a CME (e.g., Yashiro et al. 2008). The triggering mechanism of a CME itself, however, is most likely determined by the involved magnetic field topology of both the unstable CME structure and its AR environment.

CMEs are termed “homologous” when they originate from the same region within an AR and exhibit a close morphological resemblance in coronal and coronagraphic observation

(Zhang & Wang 2002; Chertok et al. 2004; Kienreich et al. 2011; Li & Zhang 2013). However, CMEs may originate from different parts of an AR and/or even have different appearances. Following Wang et al. (2013), we use the term “quasi-homologous (QH)” CMEs to denote subsequent CMEs that originate from the same AR, but disregarding their detailed magnetic source locations and appearances.

Statistical analysis of the waiting times of QH CMEs has been performed by Chen et al. (2011) and Wang et al. (2013) in order to explore the physical nature of their initiation. The waiting time is defined as the time interval between the first appearance of a CME and that of its immediate predecessor in coronagraphic images. The waiting time distribution for QH CMEs observed during 1997–1998 consists of two components separated by 15 hr, where only the first component clearly exhibits the shape of a Gaussian, peaking around 8 hr (Chen et al. 2011). This is significantly different from the waiting times of CMEs in general, appearing in the form of a Poisson distribution (Moon et al. 2003b). When only considering the QH CMEs that originated from the super ARs in solar cycle (SC) 23, the separation between the two components increases to about 18 hr, while the peak of the first component shifts to 7 hr (Wang et al. 2013). CMEs with waiting times less than 18 hr, i.e., the ones that contribute to the Gaussian component, are thought to have a close physical connection.

In addition, numerical simulations reveal that successive eruptions from a single AR may be driven by continuous shearing motions on the photosphere, the emergence of twisted magnetic flux tubes, reconnection between emerging and preexisting flux systems, or perturbations induced by a preceding eruption (e.g., DeVore & Antiochos 2008; MacTaggart & Hood 2009; Soenen et al. 2009; Török et al. 2011; Chatterjee & Fan 2013).

Most CME-productive ARs exhibit a complex photospheric magnetic field configuration, consisting of a mix of flux concentrations. Adjacent flux concentrations with opposite polarities, which may hold a flux tube, are separated by a polarity inversion line (PIL). Depending on the polarity pairs present within an AR, a number of PILs (of different length and shape) may be present. Note that in some conditions multiple polarity pairs are closely located in the vicinity of each other, with same polarity placed at the same side, forming a long PIL, i.e., a long PIL may be spanned by more than one flux tube and thus may be divided into different parts. Based on this, Chen et al. (2011) envisaged three possible scenarios for QH CMEs to occur: successive CMEs may originate (i) from exactly the same part of a PIL, (ii) from different parts of the same PIL, or (iii) from different PILs within the same AR. The first scenario has been envisaged as the recurring release of quickly replenished magnetic energy/helicity. The other two have been regarded as scenarios where neighboring flux tubes, either spanning different parts of a common long PIL or spanning distinctly different PILs, are disturbed, become unstable, and erupt. Since the peak value of the waiting time distribution may represent the characteristic timescale of the most probable involved physical process (either recurring release of the magnetic free energy or destabilization), we further explore the database of Wang et al. (2013) in this work, in order to depict the most probable scenarios for QH CMEs to occur.

2. Identification and Classification of QH CMEs

2.1. Event Sample

The event sample of Wang et al. (2013) consists of 281 QH CMEs that originated from 28 super ARs in SC 23. The CMEs are all listed in the *SOHO/LASCO* CME catalog⁷ (Yashiro 2004), and their source ARs have been determined,⁸ following the process described in Wang et al. (2011). It is based on a combination of flares and EUV dimmings or waves, as they are strong evidence for the presence of CMEs. In particular, in the present work, we use localized flare-associated features, such as flare kernels, flare ribbons, and post-flare loops in order to determine the (portions of the) PIL relevant to the individual CME.

Another two well-studied CME-rich ARs, NOAA AR 11158 and 11429, are added into the sample for detailed case study, as they were observed during the *SDO* (Pesnell et al. 2012) era, allowing an in-depth study of the associated flare emission using coronal imagery from AIA (Lemen et al. 2012) and the involved coronal magnetic field structure and evolution based on vector magnetic field measurements from HMI (Schou et al. 2012; Hoeksema et al. 2014). Out of all of the events, 188 QH CMEs exhibit a waiting time of less than 18 hr; thus, we assume them to be physically connected.

Due to limitations in the observational data, not all of the 188 QH CME events could be successfully assigned to one of the three categories introduced above, i.e., whether to originate, from the exactly same portion of a PIL, from different portions of the same PIL or from a different PIL within the same AR as their predecessor. The CMEs assigned to the first category (the latter two categories) are defined as S-type (D-type) QH CMEs. Note that QH CMEs were assigned to the second category only

when they originated from totally different portions of a long PIL (with non-overlapped post-flare loops, ribbons, etc.). In total, we were able to clearly identify the magnetic sources of 142 QH CMEs. Among them, 90 are classified as S-type, accounting for 63%; 52 are classified as D-type, accounting for 37%. Selected QH CMEs are discussed in detail in the following two subsections, in order to demonstrate the identification process. The preceding CME is referred to as CME1, and the following CME is referred to as CME2. The associated flares are accordingly referred to as flare1 and flare2.

2.2. Examples of S-type QH CMEs

S-type QH CME from NOAA AR 9026. NOAA AR 9026, observed in the form of a large bipolar sunspot region with a δ -spot (Figure 1(a)), was a highly CME-productive AR that launched at least 12 CMEs during its disk passage. Note that the strong positive polarity at $[-300'', 320'']$ in Figure 1(a) belongs to AR 9030. Figure 1 shows the magnetic source location, morphology, and time evolution of an S-type CME and its predecessor that both originated from the main PIL, located within the yellow box L1 in Figure 1(a). Figures 1(b)–(d) show the evolution of the CME1-associated M7.1 flare1, as observed by *TRACE* (Handy et al. 1999) at 1600 Å, while the white-light appearance of CME1 in *LASCO/C2* (Brueckner et al. 1995) is shown in Figure 1(e). Figures 1(f)–(i) show the corresponding features of CME2 and its associated X2.3 flare2. From Figure 1 it is evident that the chromospheric ribbons of both flare1 and flare2 appear and evolve along the same part of the main PIL of the AR. Thus, CME2, with a waiting time of 1 hr, is classified as an S-type CME.

S-type QH CME from NOAA AR 9236. NOAA AR 9236 produced more than 15 CMEs during its disk passage. The AR hosted a δ -spot of positive polarity surrounded by scattered elements of negative polarity (see Figure 2(a)). The PIL of interest is located within the yellow box L1. The two CMEs (see Figures 2(e) and (i)) were associated with an X2.3 and an X1.8 flare, respectively. The corresponding *TRACE* 1600 Å observations (Figures 2(b)–(d) and (f)–(h), respectively) reveal that the ribbons of the two flares appeared at the same location. CME2 had a waiting time of 7 hr and is thus classified as an S-type event. Note that these two CMEs were also classified as homologous events in Zhang & Wang (2002) and Chertok et al. (2004).

S-type QH CME from NOAA AR 11158. NOAA AR 11158 was the first super AR in SC 24 and produced more than 10 CMEs during disk passage. A pair of opposite polarities in the quadrupolar AR (outlined by the yellow box L1 in Figure 3(a)) produced a number of CMEs within 2 days. Most of the CMEs were front-side, narrow events and missed by *LASCO*. However, they were all well captured by *STEREO/COR1* (Kaiser et al. 2008). The CMEs shown in Figures 3(e) and (i) were associated with an M2.2 and a C6.6 flare, respectively (see Figures 3(b)–(d) and (f)–(h)). The mass ejections (marked by the white arrows in Figures 3(d) and (h)) shared the same source location. CME2, with a waiting time of 2.2 hr, is thus classified as an S-type QH CME. The cyan curve A1 in Figure 3(a) indicates the projection of the flux rope axis along the related PIL at Time1, i.e., before the occurrence of CME1. The pink curve A2 indicates the flux rope axis position at Time2, i.e., at a time instance after CME1 happened but before CME2 was launched. The lines C1 and C2 mark the position of

⁷ http://cdaw.gsfc.nasa.gov/CME_list/

⁸ http://space.ustc.edu.cn/dreams/quasi-homologous_cmes/

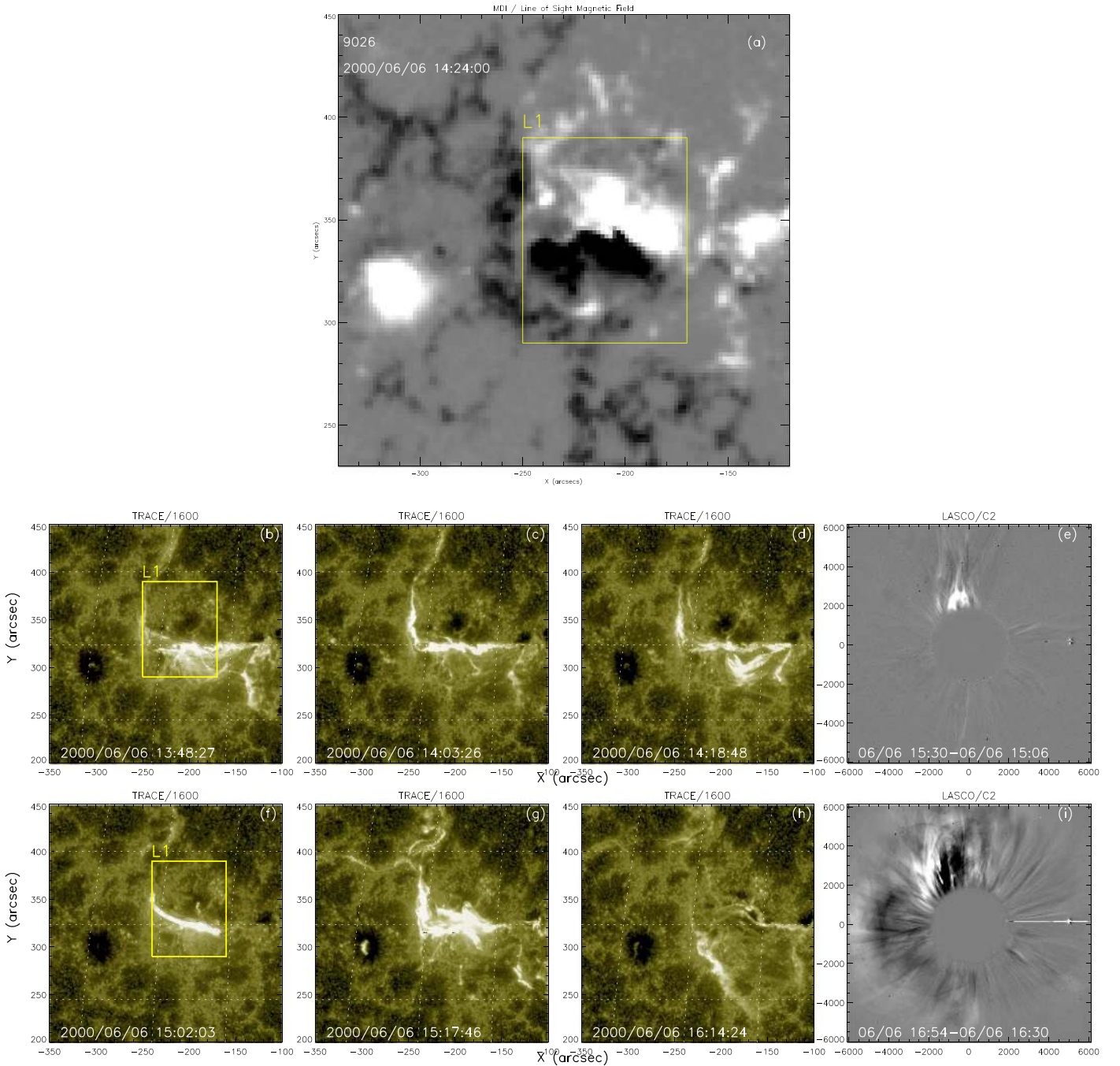


Figure 1. S-type CME and its predecessor, both originating from AR 9026. (a) *SOHO*/MDI photospheric LOS magnetic field. Black/white color represents negative/positive magnetic polarity. The yellow box L1 outlines the source location identified for the two CMEs. Panels (b)–(d) and (f)–(h) show the chromospheric flaring features associated with the preceding and following CME, respectively. Red and blue contours in (b) and (f) are drawn at $\pm[150, 850]$ G, respectively. Panels (e) and (i) show the white-light signatures of the two QH CMEs.

(An animation of this figure is available.)

two vertical cuts that will be used to derive some flux rope parameters at the two time instances. For details see Section 3.2.

2.3. Examples of D-type QH CMEs

D-type QH CME from NOAA AR 10030. NOAA AR 10030 adhered to a quadrupolar configuration (see Figure 4(a)) and produced at least eight CMEs during disk passage. A CME and its QH predecessor are shown in Figures 4(i) and (e). The yellow boxes L1 and L2 in Figure 4(a) enclose the pairs of opposite polarities, relevant to the respective CMEs, CME1 and

CME2, and defining the accordingly relevant PILs (PIL1 and PIL2, respectively). CME1 was accompanied by an X3.0 flare (see Figures 4(b)–(d)). Though an extra ribbon appeared in the positive polarity in L2 in Figure 4(b), the helical structure marked by the white arrow in Figure 4(b) and the observed chromospheric ribbons support that CME1 originated from L1. Figures 4(f)–(h) show the time evolution of the chromospheric ribbons of the CME2-associated M1.8 flare2, clearly aligned with PIL2. CME2, with a waiting time of 1 hr, thus is classified as a D-type CME. Already Gary & Moore (2004) demonstrated

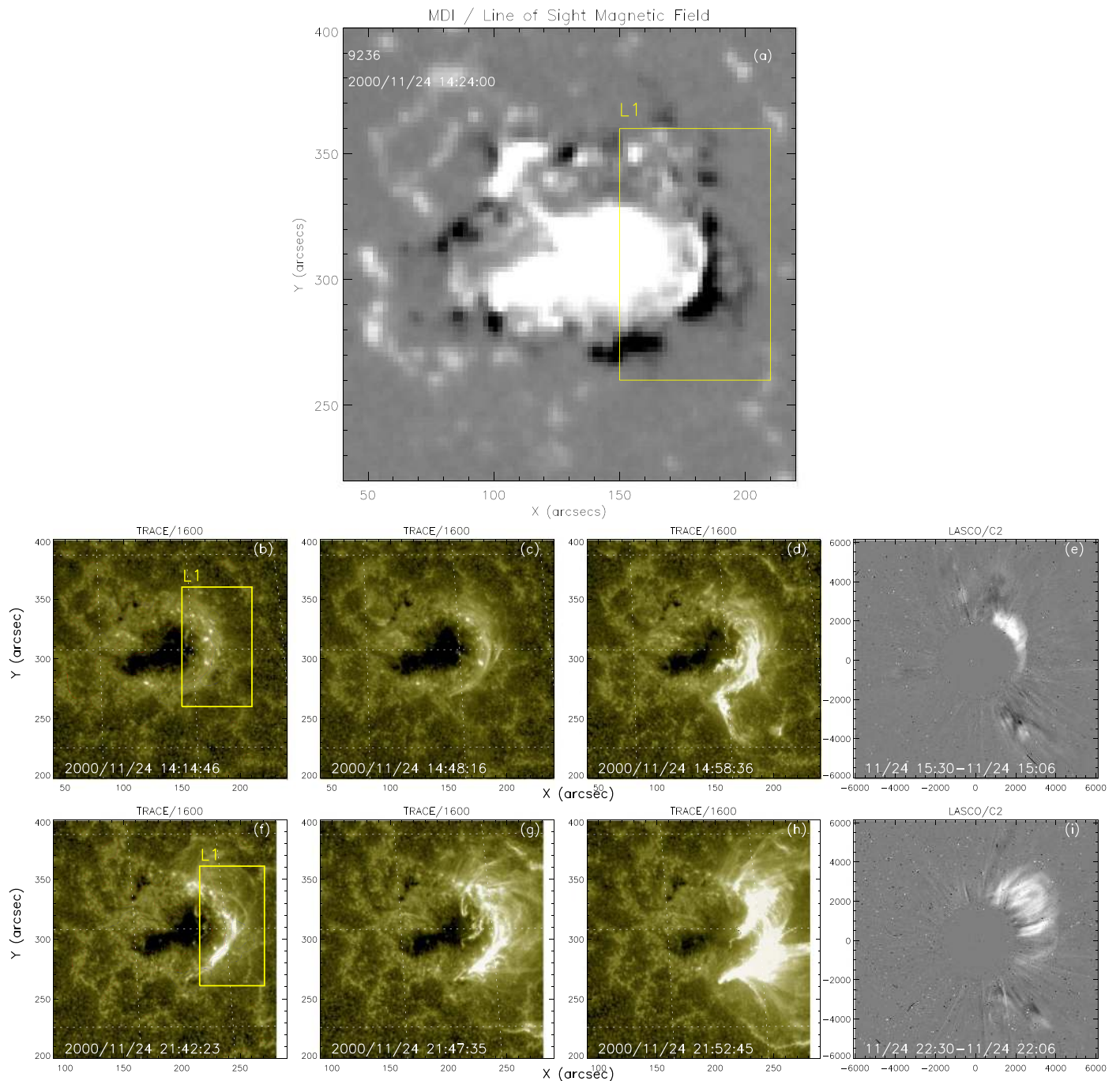


Figure 2. S-type CME and its predecessor from AR 9236. Same layout as Figure 1. (An animation of this figure is available.)

that the two CMEs should have originated from two different magnetic flux tube systems, and further argued that the observational signatures matched a breakout scenario.

D-type QH CME from NOAA AR 10696. NOAA AR 10696, similar to NOAA 9236, consisted of a concentrated negative-polarity region surrounded by scattered small positive-polarity patches (see Figure 5(a)). It produced more than 12 CMEs. The yellow boxes L1 and L2 in Figure 5(a) mark the source locations of CME1 and CME2, respectively. Figures 5(b)–(d) and (f)–(h) show the evolution of the associated M5.0 and M1.0 flare, respectively. Figures 5(e) and (i) show the appearance of the CMEs in *LASCO/C2*. The white arrows in

Figures 5(d) and (h) mark the post-flare loops associated with the two CMEs, further supporting that they originated from different flux tube systems. CME2 had a waiting time of 2.8 hr and is therefore classified as a D-type QH CME.

D-type QH CME from NOAA AR 11429. NOAA AR 11429, a super AR in SC 24, produced more than 12 CMEs during disk passage. The AR exhibited a complicated topology with a δ -spot. The two yellow boxes L2 and L1 in Figure 6(a) mark the magnetic source locations of a CME and its QH predecessor. The cyan curve A1 indicates the projection of the flux rope axis along PIL2 at Time1, i.e., before the occurrence of CME1. The cyan line C1 marks the position of a

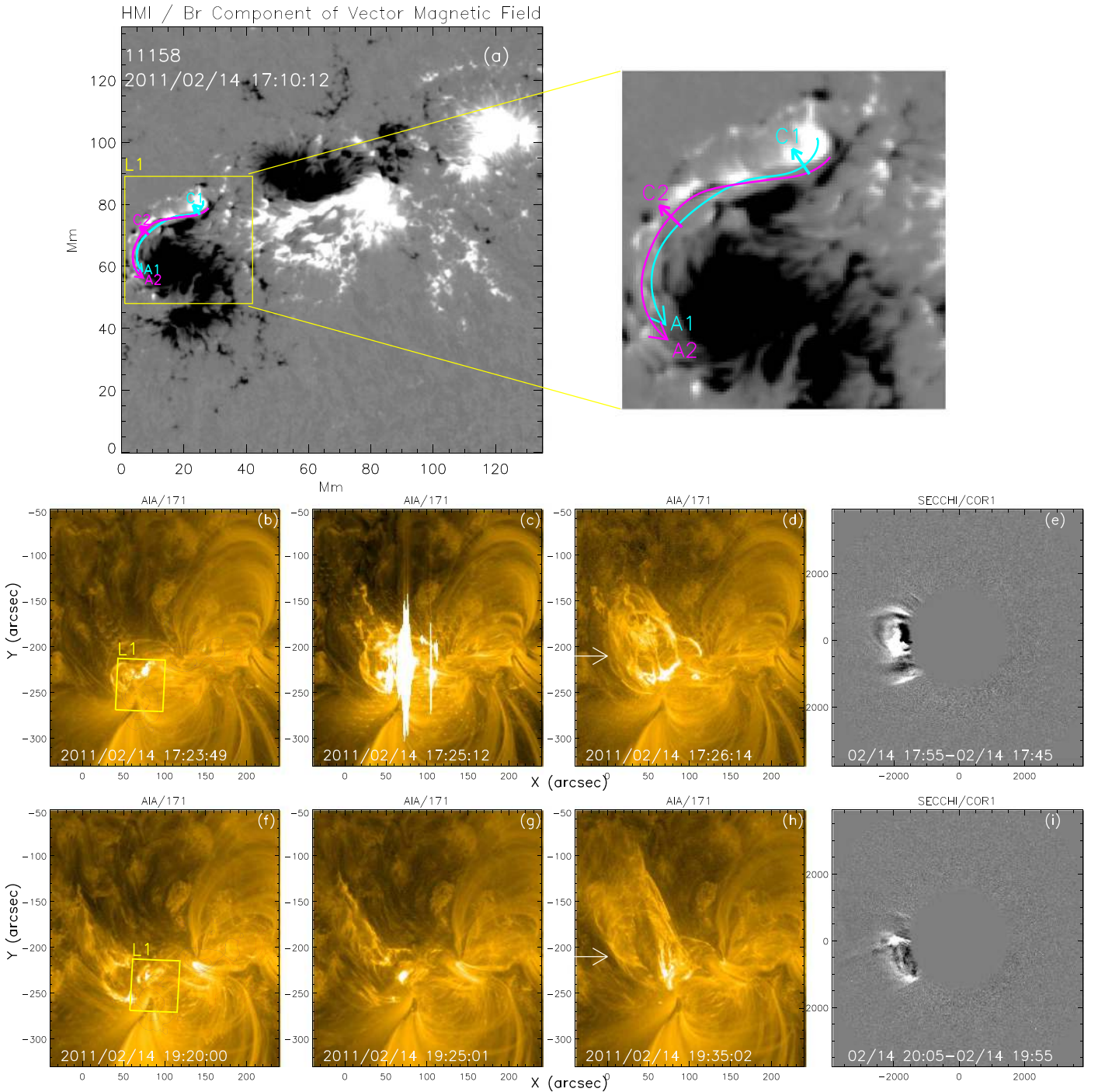


Figure 3. S-type QH CME and its predecessor that originated from NOAA AR 11158. Same layout as Figure 1. The source location L1 in panel (a) is enlarged and shown in the right top panel. Panels (b)–(d) and (f)–(h) show *SDO/AIA* 171 Å observations of the associated flares. The white arrows in panels (d) and (h) indicate the erupting mass of the two CMEs. Panels (e) and (i) show running-difference *STEREO/COR1* images. The colored lines, labeled A1 and A2 in panel (a), outline the orientation of the axes of the magnetic flux ropes, which erupted to produce the associated CMEs. C1 and C2 mark the footprints of two vertical planes used to visualize the topological properties of the involved magnetic structures. Cyan and pink represent the configurations at Time1 and Time2, respectively. (An animation of this figure is available.)

vertical plane that is perpendicular to A1 at Time1. The pink curves A2 and C2 are the corresponding axis and plane for PIL2 at Time2, i.e., a time instance after CME1 happened but before CME2 was launched. See more details in Section 3.3. The time evolution of the flares that accompanied the two CMEs, an X5.4 and an X1.3 flare, is shown in Figures 6(b)–(d) and (f)–(h), respectively. The white arrow in Figure 6(h) marks the post-flare loops of CME2, while the black arrows in

Figures 6(f)–(h) mark the post-flare loops of CME1. CME2, with a waiting time of 1 hr, is classified as a D-type CME, in agreement with its classification by Chintzoglou et al. (2015).

2.4. Waiting Time Distribution

The waiting time distribution of the 188 CMEs (with waiting times < 18 hr) is shown as a black curve in Figure 7, exhibiting

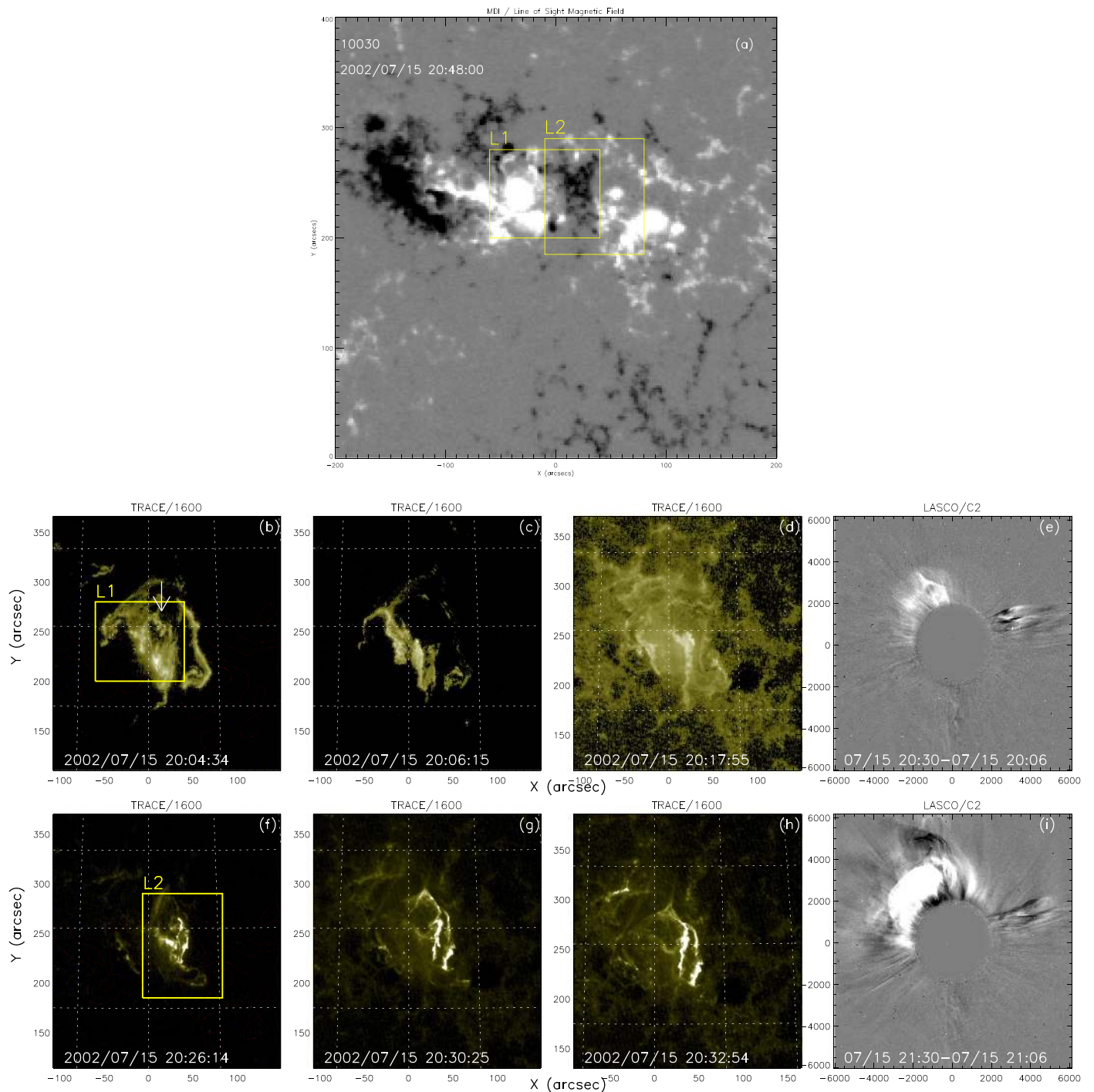


Figure 4. D-type CME and its predecessor, originating from NOAA AR 10030. Same layout as in Figure 1. The yellow boxes L1 and L2 in panel (a) outline the source location of CME1 and CME2, respectively. The white arrow in panel (b) marks an erupting helical structure.

(An animation of this figure is available.)

a Gaussian-like distribution with a peak at about 7.5 hr, suggesting that they are physically related. The distributions of precisely located S- and D-type QH CMEs are shown as a blue curve and a red curve in Figure 7, respectively. The two are distinctly different from each other: the former peaks at 7.5 hr, while the latter peaks at 1.5 hr, strongly supporting that these two types of QH CMEs may be involved in different physical mechanisms. Another slightly lower peak appears around 9.5 hr in the waiting time distribution of D-type QH CMEs. One possible reason is that in some cases, a CME triggers a

D-type QH CME in a short interval of around 1.5 hr, after which the first CME's source region undergoes an energy replenishment and produces another QH CME with an interval around 7.5 hr. However, the third CME would be classified as a D type, as it originates from a different source location from its predecessor, with a waiting time of around 6 hr. Considering the 3 hr bin size of the distribution, a peak around 9 hr may be reasonable. Another possible reason is that those D-type QH CMEs with waiting times around 9.5 hr may follow a different mechanism from the ones with short waiting times (around

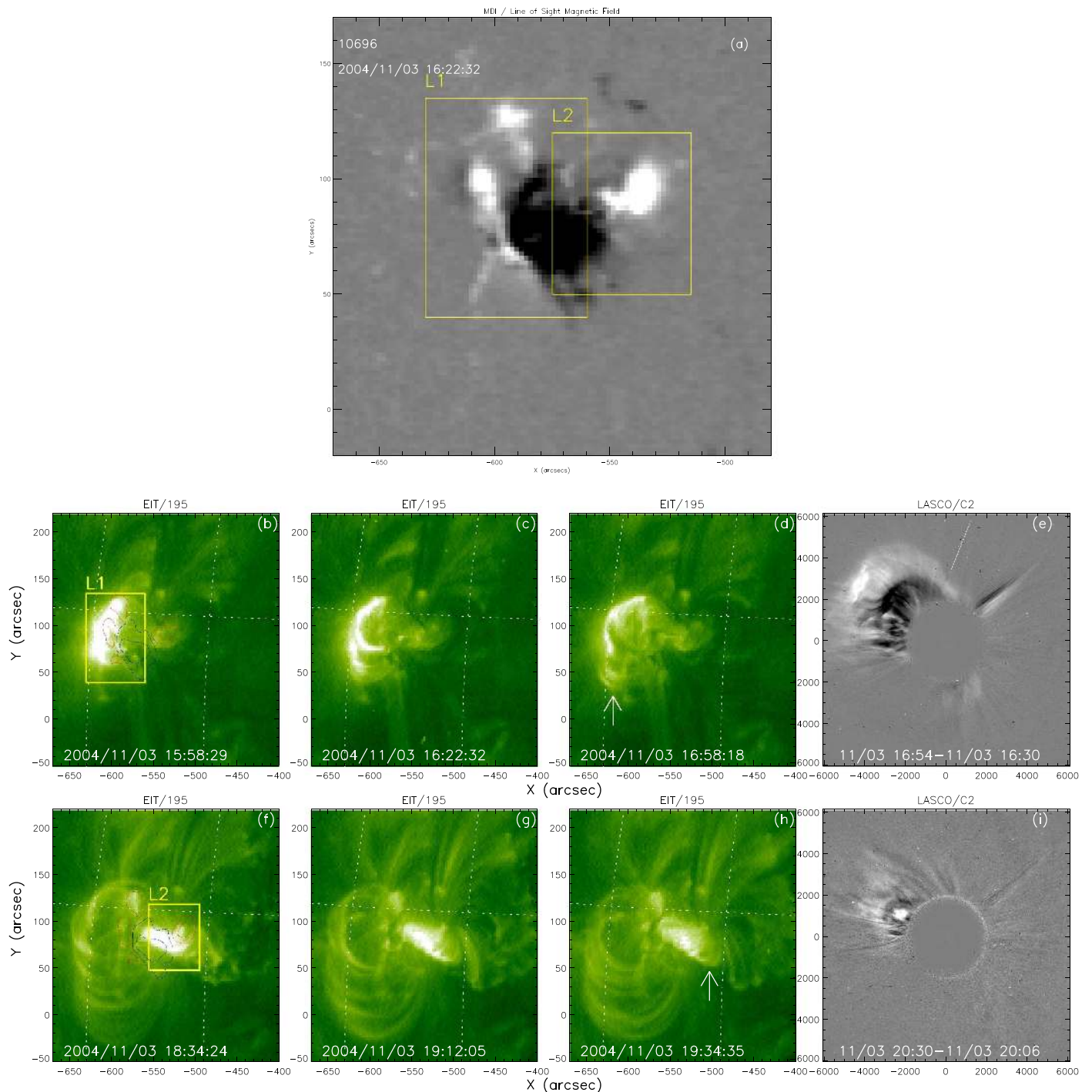


Figure 5. D-type CME and its predecessor from NOAA AR 10696. Same layout as in Figure 4. Panels (b)–(d) and (f)–(h) show the flaring features associated with the first and second CME, respectively, as observed by *SOHO*/EIT at 195 Å. The white arrows in panels (d) and (h) indicate the post-flare loops associated with flare1 and flare2, respectively.

(An animation of this figure is available.)

1.5 hr). This work aims to find the most possible (but not only) scenario for the two types of QH CMEs.

In order to explore the different underlying mechanisms, the aforementioned S-type CME in AR 11158 and D-type CME in AR 11429 are analyzed in detail in the next section. These two cases were observed during the *SDO* era, allowing for sophisticated modeling of the 3D coronal magnetic field, based on the measurements of the photospheric magnetic field vector at a high spatial resolution from *SDO*/HMI.

3. Coronal Magnetic Field Topology of S- and D-type CMEs

3.1. Method

It is widely accepted that the expulsion of a CME is determined by the inner driving force (associated with, e.g., an erupting flux rope) and the external confining force (exerted by the large-scale, surrounding coronal magnetic field; e.g., Wang & Zhang 2007; Liu 2008; Schrijver 2009). In order to investigate

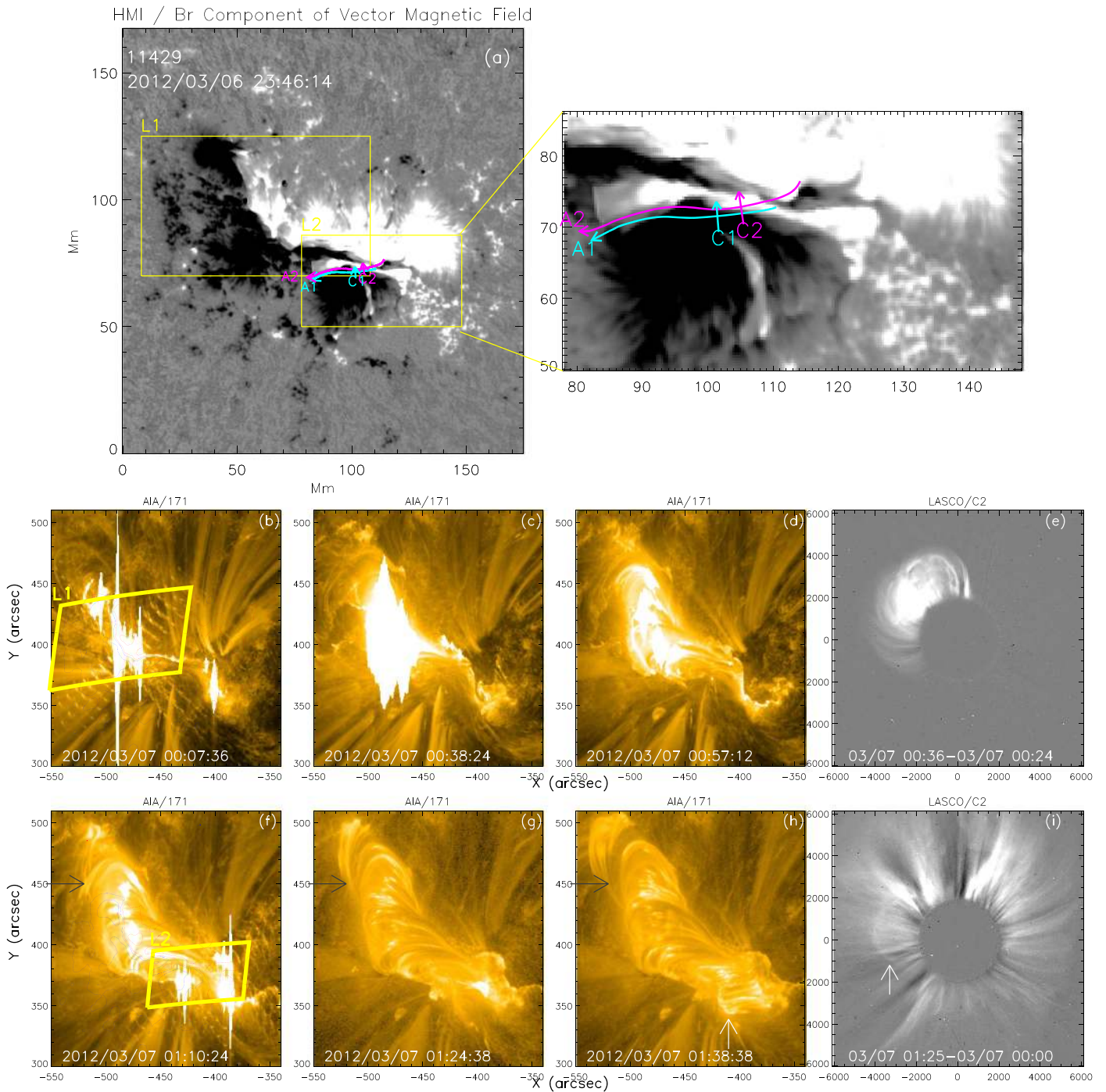


Figure 6. D-type CME and its predecessor from NOAA AR 11429. Same layout as in Figure 4. The colored lines and arrows in panel (a) have the same meaning as the ones in Figure 3. Panels (b)–(d) and (f)–(h) show the corresponding flaring features observed by *SDO/AIA* at 171 Å. The white arrow in panel (h) marks the post-flare loops of flare2, while the one in panel (i) marks the faint front of CME2. The black arrows in panels (f)–(h) mark the afterglow of flare1.

(An animation of this figure is available.)

the involved mechanisms, the knowledge of the 3D coronal magnetic field is necessary. A method developed by Wiegmann (Wiegmann 2004; Wiegmann et al. 2012) is employed for the two selected cases, to reconstruct the 3D potential (current-free) and nonlinear force-free (NLFF) fields in the corona, based on the surface magnetic vector field measurements from HMI.

A magnetic flux rope, characterized by magnetic fields twisted about a common axis, may become unstable and act as a driver for an eruption (e.g., Amari et al. 1999; Török & Kliem 2005). A flux

rope can be identified using a combination of topological measures deduced from the employed NLFF models, e.g., in the form of the twist number T_w and the squashing factor Q (Liu et al. 2016b). T_w gives the number of turns by which two infinitely approaching field lines, i.e., two neighboring field lines whose separation could be arbitrarily small, wind around each other, and it is computed by

$$T_w = \frac{1}{4\pi} \int_L \alpha dl, \quad (1)$$

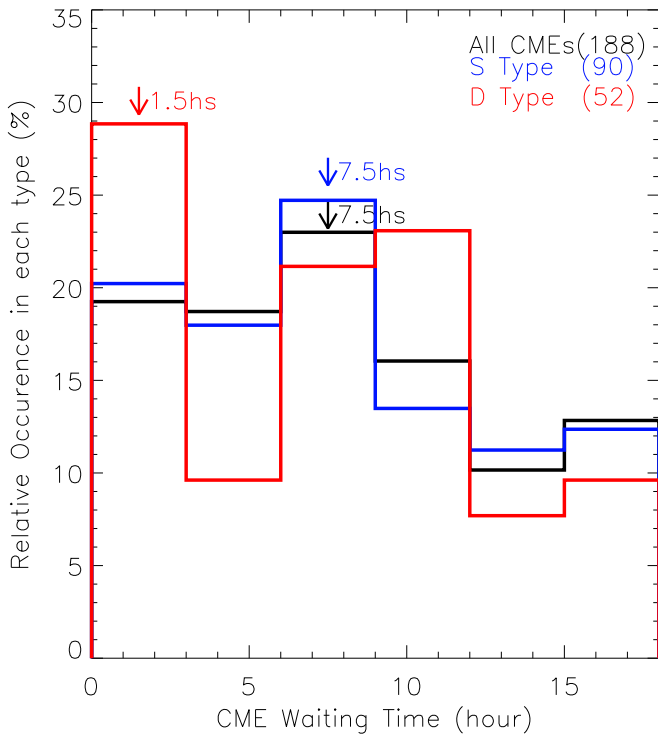


Figure 7. Waiting time distributions for the 188 QH CMEs under study, exhibiting waiting times of <18 hr (black line). The blue and red lines represent the waiting time distributions for the S- and D-type events, respectively. Numbers in parentheses denote the number of QH CMEs in the corresponding sample. Vertical arrows indicate the peak in the respective distribution.

where α is the force-free parameter, dl is the length increment along a magnetic field line, and L is the length of the field line (Berger & Prior 2006; Liu et al. 2016b). Q is a measure of the local gradients in magnetic connectivity; regions with high values of Q are referred to as quasi-separatrix layers (QSLs; Titov et al. 2002; Titov 2007).

The cross section of a flux rope with twisted field lines treading the plane would be visible as a region of strong T_w enclosed by a surface of high Q values separating the magnetic fields of the flux rope from its magnetic environment. The location of the local extremum T_w in the cross section of a coherent flux rope is a reliable proxy of the location of its central axis. Additionally, a cross section perpendicular to the axis of the flux rope (e.g., the section at the apex point of the flux rope axis) would allow the axis to run through the plane horizontally, so that the in-plane vector field will show a clear rotational pattern around the axis, which is represented by the point where T_w is maximal.

The external confining force can be measured by the decay index

$$n = -\frac{d \ln B_{\text{ex}}(h)}{d \ln h}, \quad (2)$$

where h is the radial height from the solar surface and B_{ex} is the horizontal component of the strapping potential field above the AR. Basically, n measures the run of the strapping field's confinement with height. Theoretical works predict the onset of torus instability when n is in the range of [1.5, 2.0] (Kliem & Török 2006), while observations of eruptive prominences suggest a critical value $n \sim 1$ (Filippov 2013; Su et al. 2015). It

is suggested that the former value is representative for the top of the flux rope axis, while the latter value is typical for the location of magnetic dips that hold the prominence material (Zuccarello et al. 2016). Therefore, $n = [1, 1.5]$ are used as critical decay index values for our analysis. Torus instability sets in once the axis of the flux rope reaches a height in the corona at which the strapping potential fields decrease fast enough (Török & Kliem 2005); thus, the vertical distribution of n , along the axis of the flux rope, will hint at its instability.

Since a physical relation is assumed to exist between the QH CMEs (CME2 and its predecessor, CME1), we may expect a change in the magnetic field configuration of the CME2's source location after CME1, detectable in the form of a change of the related parameters defined above (T_w , Q , and n). Therefore, we deduce these parameters from the NLFF models (for T_w and Q) and potential models (for n) of the pre-CME1 and post-CME1 (i.e., pre-CME2) corona as follows:

1. Locate the axis of the flux rope using the method of Liu et al. (2016b), which calculates the twist maps in many vertical planes and traces the field line running through the peak T_w point at each map. All traced field lines should be coinciding with each other if a coherent flux rope is present. The line is then considered to represent the flux rope axis.
2. Calculate T_w and Q in a vertical plane perpendicular to the flux rope axis. The in-plane vector field, \mathbf{B}_{\parallel} , can provide additional evidence of the presence of a flux rope in the form of a clear rotational pattern, centered on the flux rope axis position.
3. Calculate the decay index n in a vertical plane, aligned with the flux rope axis and extending from the flux rope axis upward, as a function of height in the corona.

Using the above-introduced models and concepts, we investigate the pre-CME1 and post-CME1 (pre-CME2) coronal magnetic field configuration of the two mentioned cases in NOAA AR 11158 (Section 3.2) and 11429 (Section 3.3) in great detail. The quality of the NLFF extrapolation in this paper is shown in Appendix A.

3.2. S-type QH CME from NOAA AR 11158

As demonstrated in Section 2.2, the S-type CME and its predecessor originated from the same PIL within NOAA 11158. We study the magnetic parameters at the CMEs' source location (L1) at two time instances: once before CME1, at 2011-02-14T17:10:12 UT (Time1), and once after CME1 but before CME2, at 2011-02-14T18:10:12 UT (Time2).

At both times, we find a flux rope structure from the constructed corona field (see Figures 8(g) and (h)). The magnetic properties of the pre- and post-CME1 flux rope in a vertical plane perpendicular to its axis are shown in Figures 8(a)–(c) and (d)–(f) (from left to right: Q , T_w , and \mathbf{B}_{\parallel}), respectively. The footprints of the vertical planes at the two times are marked as C1 and C2 in Figure 3(a). Their vertical extensions are indicated by the yellow lines in Figures 8(g) and (h). At Time1 (pre-CME1), a region of strong twist (Figure 8(b)) is surrounded by a pronounced Q -surface (Figure 8(a)). The diamonds in Figures 8(a)–(c) mark the location where T_w is strongest, at $T = -1.94$, and are assumed to represent the 3D location of the flux rope axis, at a coronal height of $h \gtrsim 2$ Mm. The in-plane vector magnetic fields, \mathbf{B}_{\parallel} (Figure 8(c)), show a clear rotational

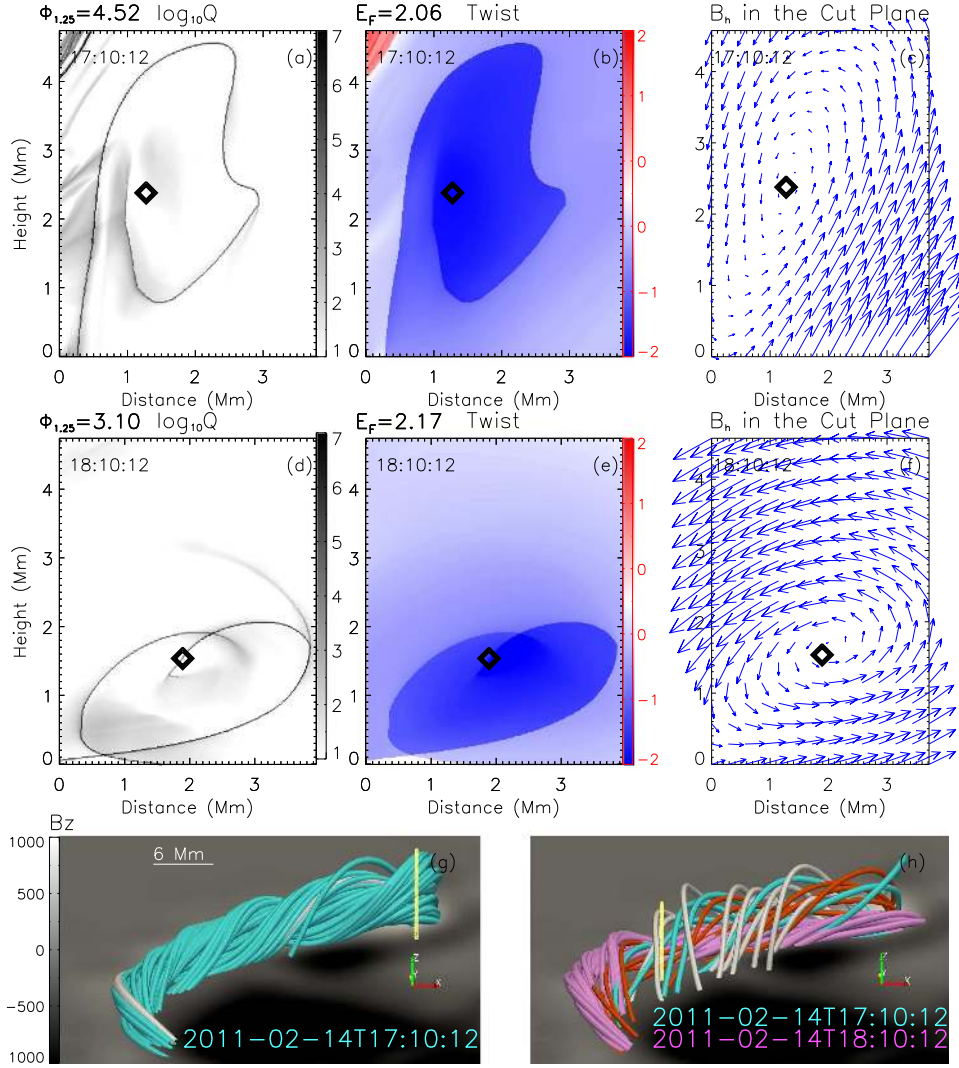


Figure 8. Pre- (at Time1) and post-CME1 (at Time2) conditions in NOAA AR 11158. Panels (a), (b), and (c) show Q , T_w , and B_{\parallel} , respectively, in a vertical plane perpendicular to the pre-eruptive flux rope axis. The footprint of the plane is indicated by the colored line C1 in Figure 3(a). Panels (d)–(f) show the distribution of the same quantities at Time2, in a plane perpendicular to the flux rope axis (C2 in Figure 3(a)). The yellow lines in panels (g) and (h) mark the positions and extents of the vertical planes. The blue arrows in (c) and (f) indicate the vector fields with the normal components going into the plane. The black diamonds in (a)–(f) mark the position where T_w has its maximum. Panels (g) and (h) show the twisted field lines, traced based on the geometrical information in the Q and T_w maps. Cyan and pink lines mark the flux rope field lines at Time1 and Time2, respectively. The white line in panel (g) indicates a representative field line in the BP, while the white field lines in panel (h) show the arcade traced in the post-CME1 corona, but from exactly the same coordinates as the upper part of the flux rope at Time1. The cyan field lines in panel (h) roughly outline the flux rope at Time1 for comparison. The red lines in panel (h) are also some pre-CME1 flux rope field lines, but traced exactly from the coordinates of the high- T_w region at Time2 (panel(e)). $\Phi_{1.25}$, given at the headers of panels (a) and (d), are vertical magnetic flux (in units of 10^{19} Mx) from the strong T_w region ($|T_w| \gtrsim 1.25$) at each time, respectively. E_F , given at the headers of panels (b) and (e), are free magnetic energy (in units of 10^{32} erg) at the two times. The grayscale bar at the left of panel (g) shows the scale of the photospheric magnetic fields plotted in panels (g) and (h), in units of gauss.

pattern, centered around the flux rope axis, suggesting a left-handedness of the flux rope, since the blue arrows indicate the vector fields with the normal components going into the plane. The field lines passing through the strong twisted region are shown in Figure 8(g) in cyan, even adhering to a Bald Patch (BP), a set of field lines that graze the photosphere at the PIL (see, e.g., Titov et al. 1993). A representative field line in the BP is plotted as a white line, which is determined by the criteria introduced in Titov & Démoulin (1999, Equation (32)).

At Time2 (post-CME1), the highest value of twist in the vertical plane perpendicular to the flux rope axis is found as $T_w = -2.11$, marked by the diamonds in Figures 8(d)–(f). Again, a region of strong twist (Figure 8(e)) is surrounded by a pronounced Q -surface (Figure 8(d)), but located lower in the model corona (height of the flux rope axis $h \lesssim 2$ Mm). The

fields traced from the high- T_w region are shown in Figure 8(h) as pink curves. For comparison, the outline of the flux rope at Time1 is shown again as cyan curves. The more potential arcade fields (white lines) are traced at Time2 but from the coordinates of the top of the flux rope at Time1.

The direct comparison between the pre- and post-CME1 model magnetic field configuration suggests that the upper part of the flux rope might erupt during CME1, while the lower-lying part of the flux rope seems to remain. In order to check the conjecture, we further trace the field lines within the pre-CME1 corona from exactly the same starting locations used for tracing the post-CME1 flux rope (i.e., the high- T_w region enclosed by the high- Q boundary at Time2; see Figures 8(d) and (e)). The traced pre-CME1 field configuration (red lines in Figure 8(h)) clearly differs from the post-CME1 field structure

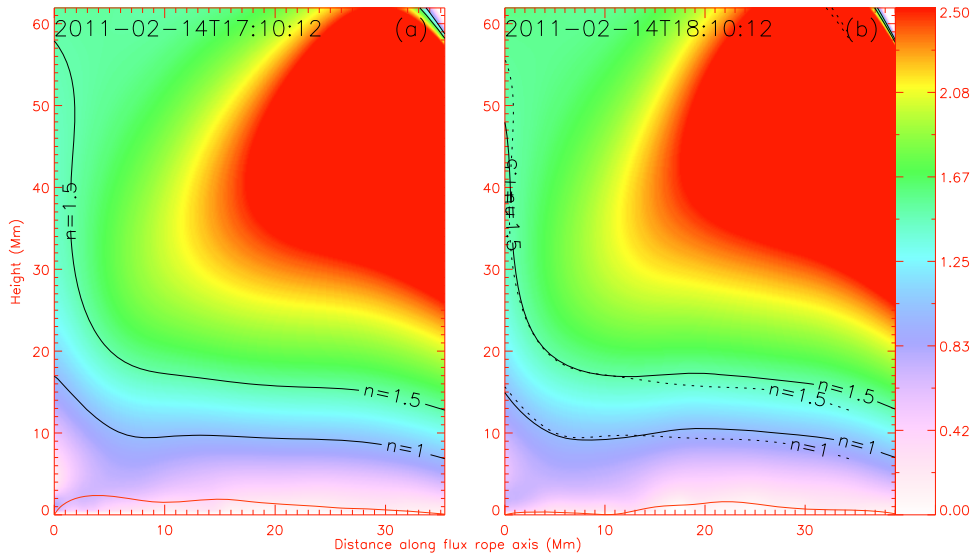


Figure 9. Vertical distributions of the decay index, n , above the axis of the (a) pre-CME1 and (b) post-CME1 flux ropes in NOAA AR 11158. The black lines in panels (a) and (b) mark the height where $n = 1$ and $n = 1.5$, respectively, at the different time instances. The dotted lines in panel (b) mark the corresponding heights at Time1 for comparison. The red lines indicate the respective height of the flux rope axis.

(pink lines in Figure 8(h)), which may suggest two possibilities: (i) the flux rope totally erupted during CME1, after which a new one emerged, or reformed; and (ii) the flux rope underwent a topology change in which part (not simply the upper part) of it was expelled during CME1, while the other part was left, being responsible for CME2. See Appendix B for some details on CME2.

We also calculated the unsigned vertical magnetic flux from the strong T_w region in the aforementioned planes. No strong twist region exists outside of the flux rope; thus, instead of doing an image-based flux rope recognition, we directly select the regions with $|T_w| \gtrsim 1.25$. $|T_w| = 1.25$ is a threshold value for kink instability (Hood & Priest 1981; Török & Kliem 2003). The flux is calculated by

$$\Phi_{1.25} = \int_{A_{1.25}} |\mathbf{B}_\perp| dA, \quad (3)$$

in which \mathbf{B}_\perp is the magnetic field perpendicular to the vertical plane and dA is the element area. The planes are perpendicular to the axes of the pre- and post-CME1 flux ropes; thus, the vertical magnetic flux can represent the axial flux of the flux rope. The unsigned vertical magnetic flux (given at the header of Figures 8(a) and (d)) decreased from 4.52×10^{19} Mx at Time1 to 3.10×10^{19} Mx at Time2, which can be due to either ejection or simple redistribution of twisted field lines, since twist is not supposed to be conserved during the flux rope evolution. However, CME1 has been confirmed to be related to source location L1 based on observation; as discussed in Section 2.2, the decrease here is more likely to support a twist release through eruption rather than redistribution.

We cannot make a definite conclusion on whether the flux rope at Time2 is a partial eruption remnant or is a newly emerged/reformed one. However, the pre-CME1 flux rope has a BP, and the post-CME1 rope has some nearly potential loops right above it. Thus, we prefer a partial expulsion model (Gibson & Fan 2006), consisting of a coherent flux rope with a BP, to explain the eruption process: the field lines in the BP are not free to escape, so that during the writhing and upward

expansion of the ends of the field lines, a vertical current sheet may form, along which internal reconnection may occur and finally split the flux rope into two parts. The white arcades in Figure 8(h) could be the post-eruption loops, which may also support that part of the flux rope erupted with CME1.

Figures 9(a) and (b) show the distribution of the decay index n as a function of height above the flux rope axis, for Time1 and Time2, respectively. The projections of the flux rope axis at the two times are indicated by the curves A1 (for Time1) and A2 (for Time2) in Figure 3(a). The solid black lines in Figure 9 indicate the height where $n = 1$ and $n = 1.5$. It is evident that, for both time instances, the vertical run of n varies strongly along the flux rope, with the $n = 1.5$ level being located at a height above 48 Mm at one end and around 16 Mm at the other end of the flux rope. The height where $n = 1$ varies less dramatically along the flux rope and is located at the height around 10 Mm. Comparison of the $n = 1.5$ level at Time1 and Time2 (represented by the dotted and solid black curves in Figure 9(b), respectively) suggests that the critical height at the southeastern end ($x = 0$ Mm in Figure 9) is lowered by about 8 Mm. In the remaining part of the flux rope, no significant change was detected, which indicates that the external confining force was not lowered significantly by the first eruption. The critical height, both before and after CME1, was located relatively low in the solar atmosphere (e.g., $n = 1$ at $h \approx 10$ Mm), but still far above the height of the flux rope axis (red lines in Figures 9(a) and (b)), located below 3 Mm at both times. The maximal n at the flux rope axis reaches 0.80 at Time1 and 0.44 at Time2, which are both lower than the critical $n = 1.5$ for torus instability. The results argue against torus instability in triggering the two QH CMEs.

Sun et al. (2012) studied the long-term evolution of NOAA AR 11158 and showed that the fast emergence and continuous shear of a bipolar photospheric magnetic field (L1 in Figure 8) accumulated a large amount of magnetic free energy before the onset of a series of QH CMEs. They showed that the emerging fields reconnected with preexisting fields, which finally led to the eruptions. Together with our analysis, their results hint at a multistage energy release process during which the magnetic free energy is released owing to the

successive eruptions from the same bipolar region (L1 in Figure 8). Meanwhile, the energy was replenished through the shearing motion and ongoing flux emergence. We also calculate the magnetic free energy in the entire extrapolation volume at the two time instances (shown as E_F in Figures 8(b) and (e)) by

$$E_F = \int_V \frac{B_N^2}{8\pi} dV - \int_V \frac{B_P^2}{8\pi} dV, \quad (4)$$

where B_N is the NLFF field, B_P is the potential field, and dV is the element volume. E_F shows a slight increase by 5% from Time1 (2.06×10^{32} erg) to Time2 (2.17×10^{32} erg), which is against the expectation that the magnetic free energy would decrease after CME1, since CME1 should have taken part of the free energy during the multistage energy release process. The slight increase could be due to the small fraction of the big, fast-evolving AR that the erupting bipolar system accounts for, and/or the fast accumulation of the magnetic free energy by flux emergence and shear motions. Besides, the free energy calculated from the model coronal field has an uncertainty of around 10% (Thalmann et al. 2008), so that no definite conclusion on the loss of free energy during CME1 could be made here.

3.3. The D-type QH CMEs from NOAA AR 11429

As discussed in Section 2.3, a D-type CME and its predecessor originated from two different locations within NOAA 11429, separated by a waiting time of just 1 hr. A physical relation is assumed to exist between the two QH CMEs; thus, a change at the source location of CME2 after CME1 is expected (see Section 3.1). Therefore, we study the magnetic parameters at the source location (L2) of CME2 at two time instances in the following, once before CME1, at 2012-03-06 23:46:14 UT (Time1), and once after CME1 but before CME2, at 2012-03-07 00:58:14 UT (Time2).

Figure 10 shows the T_w , Q , in-plane vector field ($\mathbf{B}_{||}$) maps and the traced flux ropes for AR 11429. Through checking the T_w and Q maps in many vertical cuts across PIL2, we found three possible flux ropes at Time1. The peak T_w point resides in the middle structure; thus, we again identified the axis of the middle rope with the peak T_w point and then placed a plane perpendicular to the flux rope axis. The plane's footprint is marked as C1 in Figure 6(a), and its vertical extent is marked by the yellow vertical line in Figure 10(g). Figures 10(a)–(c) show the distribution of Q , T_w , and $\mathbf{B}_{||}$, respectively, calculated in the plane. The axis of the middle flux rope, with a peak value $T_w = 1.86$, is indicated by diamonds. The in-plane vector field, $\mathbf{B}_{||}$, displays three clearly rotational patterns with opposite handedness, alternately. This supports that there were three flux ropes present along PIL2 at Time1. A configuration with two vertically arranged flux ropes, i.e., a so-called double-decker flux rope, has been studied (Liu et al. 2012; Kliem et al. 2014). However, a similar configuration, with three flux ropes presented here, is barely reported to our knowledge; we name it a triple-decker flux rope, analogically. The blue arrows indicate the vector magnetic fields, with the vertical component going into the plane; thus, the upper one and the lower one (FR₃² and FR₂¹ in Figure 10) are left-handed (i.e., the in-plane vector field exhibits a counterclockwise sense of rotation), while the middle one (FR₂²) is right-handed. The squares and triangles in Figures 10(a) and (b) mark the position of the axes

of FR₂³ and FR₂¹, with local peak values $T_w = -1.82$ and $T_w = -1.49$, respectively. The plane is not perpendicular to the axes of FR₂³ and FR₂¹, positions of which do not correspond well with the rotational centers of the ropes' in-plane fields; thus, the symbols are not marked in Figure 10(c). Figure 10(g) depicts the structure of the flux ropes, FR₂³ in blue, FR₂² in orange, and FR₂¹ in cyan. A longer, strongly twisted rope (marked as FR₁ in Figures 10(g)–(h)) is aligned with PIL1 and results in CME1. The white lines in Figure 10(g) represent some nearly potential arcades above the flux ropes. Note that the southwestern end of FR₁ was located close to the triple-decker flux rope along PIL2, and part of the arcade field was overlying both the southwest end of the CME1-associated flux rope and the eastern part of the triple-decker flux rope. Therefore, we may assume that the eruption of FR₁ easily affected the triple-decker flux rope in various ways, e.g., by removing the common overlying arcades, disturbance, compressing the neighboring fields through expansion of the post-eruption loop system below the erupted flux rope, and even reconnecting with the neighbor fields during expansion.

At Time2 (see Figures 10(d)–(f)), the upper two flux ropes along PIL2 evidently disappeared from the extrapolated domain, while the lower one was then located higher, with a peak value $T_w = -1.81$ (indicated by triangles) located at $h \sim 6$ Mm. The whole structure also appears expanded compared to that at Time1. The in-plane vector field, $\mathbf{B}_{||}$, exhibits a rotational pattern around the maximum value of T_w , which is evidence for the presence of a flux rope (Figure 10(f)). The footprint of the vertical plane is marked as C2 in Figure 6(a), and its vertical extent is marked as a yellow line in Figure 10(h). Field lines traced from the strong T_w region at Time2 are shown in pink in Figure 10(h). For comparison, the flux rope that was present at Time1 is shown as cyan lines. Comparison of FR₂¹ at Time1 and Time2 reveals that it elevated and expanded, as well as gained internal twist. The vertical magnetic fluxes calculated by Equation (3) from the strong T_w region ($|T_w| \gtrsim 1.25$) of the lowermost structure of the triple-decker flux rope ($h \lesssim 5$ Mm at Time1 and $h \lesssim 8$ Mm at Time2), i.e., the representation of the axial magnetic flux of the lower flux rope (shown at the headers of Figures 10(a) and (d)), indicate an increase by 2.48 times (from 2.28×10^{19} Mx at Time1 to 5.66×10^{19} Mx at Time2), supporting the enhancement of the twist. The upper two flux ropes, with opposite handedness, clearly disappeared from the system with almost no remnant left behind. A QSL exists between the two ropes (strong Q line at around 8.5 Mm in Figure 10(a)). Thus, we prefer annihilation due to local reconnection that started from the QSL, rather than expulsion, to account for the absence of them at Time2. Annihilation of the ropes would cause a decrease of the local magnetic pressure, which is likely to allow FR₂¹ to rise, expand, and finally erupt, giving rise to the faint CME2.

Further support for this scenario is given by the evolution of the observed chromospheric ribbons as shown in Figure 11. At the beginning of flare1, two ribbons, labeled R₁¹ and R₁² in Figure 11(a), expand on both sides of PIL1. While R₁² grew southward in time (Figure 11(b)), two more faint and small ribbons, R₁³ and R₁⁴, became visible along PIL2 (Figure 11(c)). In comparison to the flux ropes shown in Figures 10(g) and (h), this pair of ribbons indicates the involvement of FR₂² and FR₂³ in the magnetic process. The two ribbons showed no clear sign of development that departed from or along the PIL, which may be

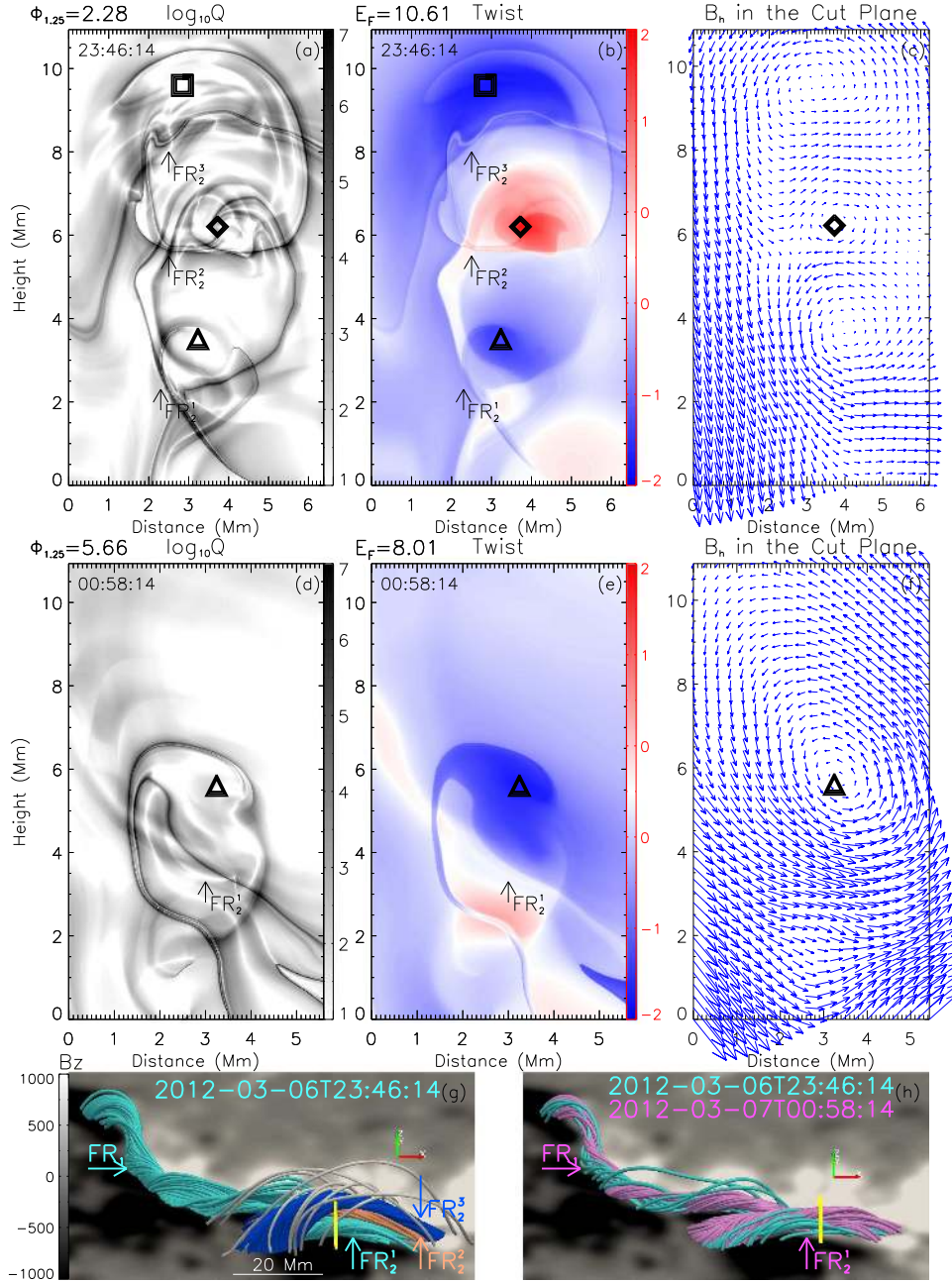


Figure 10. Magnetic features in the vertical cuts (indicated by the colored cuts C1 and C2 in Figure 6 (a)) above the PIL2 in AR 11429 at Time1 and Time2. Same layout as Figure 8. Arrows in panels (g) and (h) mark the flux rope along PIL1 as FR1, the lower (middle, upper) flux rope along PIL2 as FR₂¹ (FR₂², FR₂³); same meaning in panels (a), (b), (d), and (e). Yellow vertical lines in panels (g) and (h) mark the position of the vertical cuts. The white lines in panel (g) are some nearly potential arcades above the flux ropes. The cyan lines in panel (h) roughly outline the flux ropes at Time1. $\Phi_{1.25}$, given at the headers of panel (a) and (d), are vertical magnetic flux (in units of 10^{19} Mx) from the strong T_w region ($|T_w| \gtrsim 1.25$) of the lowermost rope at each time, respectively. E_F , given at the headers of panels (b) and (e), are free magnetic energy (in units of 10^{32} erg) at the two times.

evidence for a local, small-scale reconnection process. FR₂² and FR₂³ should have reconnected and annihilated during the first eruption. After flare1/CME1, the lower flux rope became unstable as well and erupted, giving rise to a further pair of flare ribbons, R₂¹ and R₂², at the beginning of flare2.

Note that there still existed a flux rope at PIL1 after CME1, though we cannot determine whether it is a remnant or a newly emerged/reformed one. A similar analysis is performed across PIL1. See Appendix C for details. The magnetic free energy in the extrapolated pre- and post-CME1 corona volume (shown as E_F in Figures 10(g) and (h)) shows a decrease of 25% (from 10.61×10^{32} erg at Time1 to 8.01×10^{32} erg at Time2),

which is beyond the uncertainty (10%), implying a clear energy release with CME1.

Figures 12(a) and (b) show the distribution of the decay index n as a function of height above the axis of the lower flux rope at PIL2, for Time1 and Time2, respectively. The projection of the flux rope axis at the two times is indicated by the curves A1 and A2 in Figure 6(a). The solid black curves mark the height where $n = 1$ and $n = 1.5$. The height at which $n = 1.5$ varies between $h = 30$ Mm and 50 Mm along the flux rope axis, while the height at which $n = 1$ shows a similar trend but at lower heights (about 15 Mm lower). The dotted lines in Figure 12(b) are critical heights at Time1 for

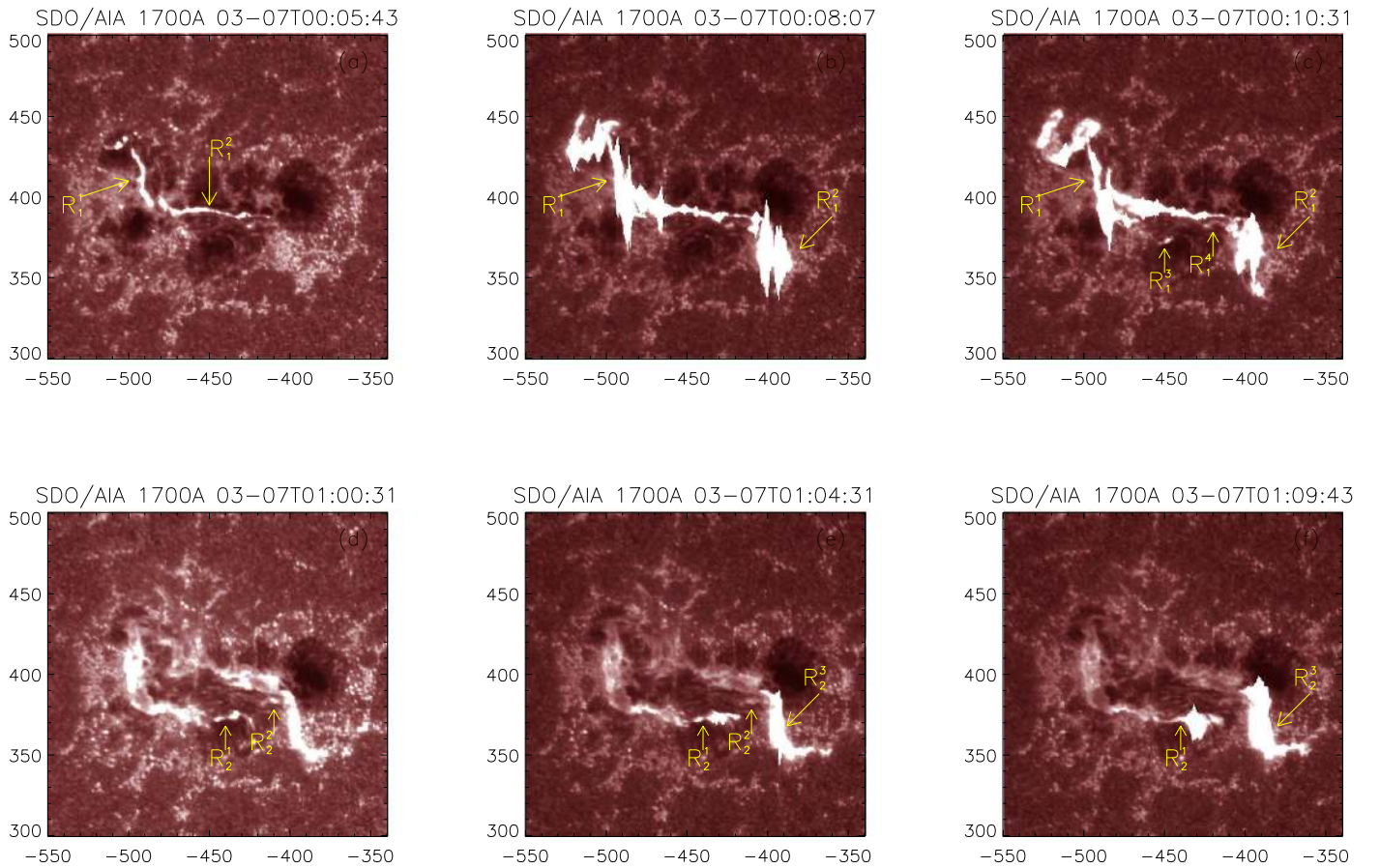


Figure 11. Evolution of flare ribbons during the two QH eruptions in AR 11429. Panels (a)–(c) are for flare1, and panels (d)–(f) are for flare2. Yellow arrows mark different ribbons during the flares. R_j^i denotes the j th ribbon for the i th flare.

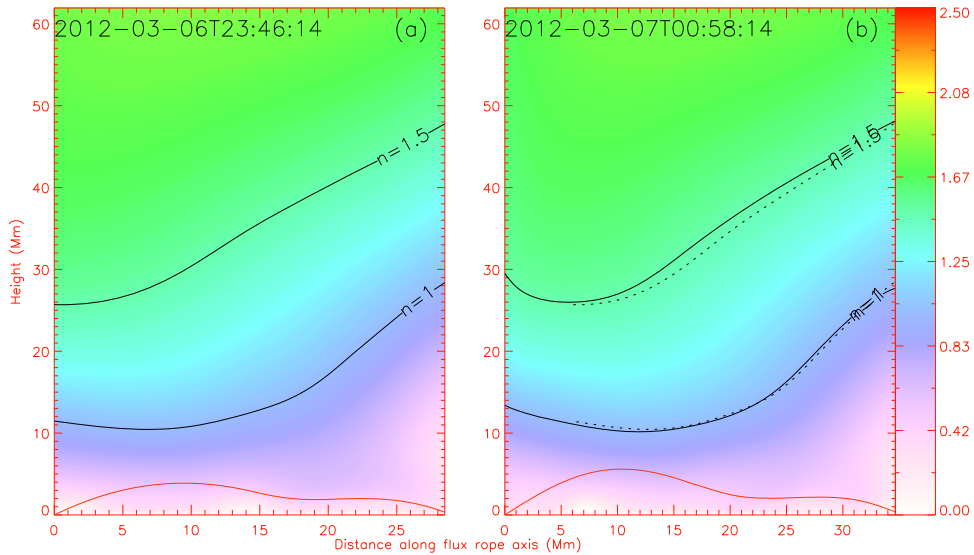


Figure 12. Decay index distribution above the axis of the lower flux rope along PIL2 for AR 11429 at Time1 and Time2. Similar layout as Figure 9.

comparison. The red lines indicate the height of the flux rope axis, which both are lower than 6 Mm at the two time instances. No significant change is found, suggesting that CME1 may not significantly lower the constraining force of the overlying field. At both times, the predicted critical height for the onset of torus instability ($n = 1.5$) is located much higher in the corona than the axis of the flux rope. In addition, the observation-based

critical height (where $n = 1$) is located clearly above the flux rope. The maximal n at the flux rope axis is 0.59 at Time1 and 0.53 at Time2, both lower than the critical value $n = 1.5$, also suggesting that torus instability may not have been the direct trigger for the two CMEs.

We conclude for the D-type CME and its predecessor from NOAA AR 11429 that their magnetic source regions were

located very close to each other and bridged by the same large-scale potential field arcade. The first occurring CME1 (associated with the flux rope along PIL1) destabilized the magnetic environment of the nearby flux tube system (above PIL2), leading to the reconnecting annihilation of the upper two flux ropes along PIL2, which decreased the local magnetic pressure and led the lower flux rope along PIL2 to rise, expand, and finally erupt as well (during flare2, and causing the associated CME2). See Appendix D for some details of CME2.

4. Summary and Discussions

In this paper, we analyze 188 QH CMEs with waiting times less than 18 hr and find that the waiting times show a Gaussian distribution peaking at about 7.5 hr. Thus, the CMEs are believed to be physically related in the statistical sense. A classification based on the precise source locations has been performed: QH CMEs that share the source locations with their predecessors are defined as S type, and the ones having different source locations from their predecessors are defined as D type. The same source location means the involvement of the same part of a PIL, and different source locations mean different parts of one PIL or different PILs in an AR. In total, we classified 90 S-type QH CMEs and 52 D-type ones. Six cases, three of D type and three of S type, are discussed in Section 2 to show the process of detailed identification, basically based on the corresponding localized flaring signatures such as ribbons and post-flare loops across the PILs.

The waiting time distributions of the two types of QH CMEs are significantly different: the distribution of the S-type CMEs peaks at around 7.5 hr, while the distribution of the D-type CMEs peaks at around 1.5 hr, suggesting that the major mechanisms of the two types of QH CMEs are probably different. In order to picture the differences in the possibly underlying mechanisms, one of the S-type cases and one of the D-type cases are analyzed in detail.

The S-type CME and its predecessor (i.e., CME2 and CME1) originated from the same location, with a waiting time of 2.2 hr in the quadrupolar AR 11158. Three parameters—the squashing factor Q ; the twist number T_w , which can locate the inner flux rope; and the decay index n , which measures the external confining force—are investigated at the erupting region at Time1 (the time instance before the CME1) and Time2 (the time instance after CME1 but before CME2). The decay index above the erupting region shows no significant change, supporting that CME1 did not weaken the external confinement significantly. Note that the coronal magnetic field is extrapolated using the photospheric magnetograms as boundaries. It is possible that the change of the magnetic field in the corona cannot feed back to the photosphere within a short duration owing to the high plasma β (ratio of gas pressure to magnetic pressure) and the long response times of the photosphere relative to the corona; thus, the decay index remains unchanged. At both time instances, the height where decay index reaches the critical value for torus instability is much higher than the height of the flux rope axis, which suggests that torus instability may not be the direct cause for the two CMEs.

The differences between the flux rope field lines that traced from the same starting coordinates in the pre- and post-CME1 corona indicate a topological change during flare1/CME1; while the reduction of the representation of the flux rope axial magnetic flux from Time1 to Time2 is evidence of an eruption,

the presence of a BP and post-eruption loop at the position of the upper part of the flux rope at Time1 is more likely to support a partial expulsion process: part of the flux rope erupted as CME1, while the other part may survive, erupting later as CME2, which fits into a free energy multistage release process. However, the magnetic free energy in the extrapolation volume almost remains unchanged, which may be due to three reasons: (i) the small extent of the CME-involved corona, compared to the entire AR for which the energy budget was estimated; (ii) ongoing free energy replenishment; and (iii) the uncertainty of the free energy estimate itself.

Besides the scenario of the S-type case in AR 11158, the eruptions from the same location can also be in an energy-consuming and replenishment process as studied in Liu et al. (2016b). Two CMEs with a waiting time of 13 hr originated from the main PIL of a bipolar AR, AR 11817. The first one erupted and took the majority of the twist of the flux rope structure (Figure 9 in Liu et al. 2016b). A very weakly twisted structure still existed after the eruption, gained the twist through continuous shear motion on the photosphere (Figure 10 in Liu et al. 2016b), and finally grew into a highly twisted seed flux rope for the next eruption. In this case, CME1 consumed most of the free energy at the erupting location, and the energy for CME2 was refilled after CME1. In the case of AR 11158, CME1 may only consume part of the free energy, and the energy regain was ongoing before and after CME1 through the shear motion and flux emergence at the PIL (Sun et al. 2012). Although the amount of the consumed energy for CME1 may be different, they both are due to continuous energy input, fitting into the energy regain scenario. The BP of the flux rope in AR 11158 is probably the reason for preventing the flux rope from a full eruption, whereas the rebuilding of magnetic free energy, e.g., flux emergence and shear motions, should be the main reason for the S-type eruptions. Detailed study of another CME-rich AR, AR 9236, which produced more than 10 S-type CMEs with a mean waiting time around 7 hr, also suggests that those S-type CMEs were caused by continuously emerging flux, supporting the free energy regain scenario (Nitta & Hudson 2001; Zhang & Wang 2002; Moon et al. 2003a).

The peak value around 7.5 hr of the S-type QH CMEs' waiting time distribution could be a characteristic timescale of the free energy replenishment process.

The D-type eruption and its predecessor originated from two different locations in AR 11429 with a waiting time of 1 hr. No significant change is found in the decay index, like that in AR 11158. Again, the heights where decay index reaches the critical value for torus instability are much higher than the heights of the flux rope axes at both time instances, arguing against torus instability in triggering the two CMEs. However, the seed flux rope for CME2, i.e., the lower flux rope at PIL2, shows a stronger twist, clear rising, and expansion after CME1, which are favorable for its eruption. The most possible reason for the change of the flux rope is that CME1 influences the magnetic environment on PIL2 that make the upper two flux ropes disappear, leading to a decrease of the local magnetic pressure and allowing the lower one to erupt. In the post-CME1 model corona, the upper two flux ropes totally disappeared from the domain. During flare1, a pair of ribbons ignited along PIL2 after the brightening of the ribbons along PIL1, with no development departing from the PIL, supporting a local reconnecting annihilation between the upper two flux ropes, rather than expulsion of them. The details about how the

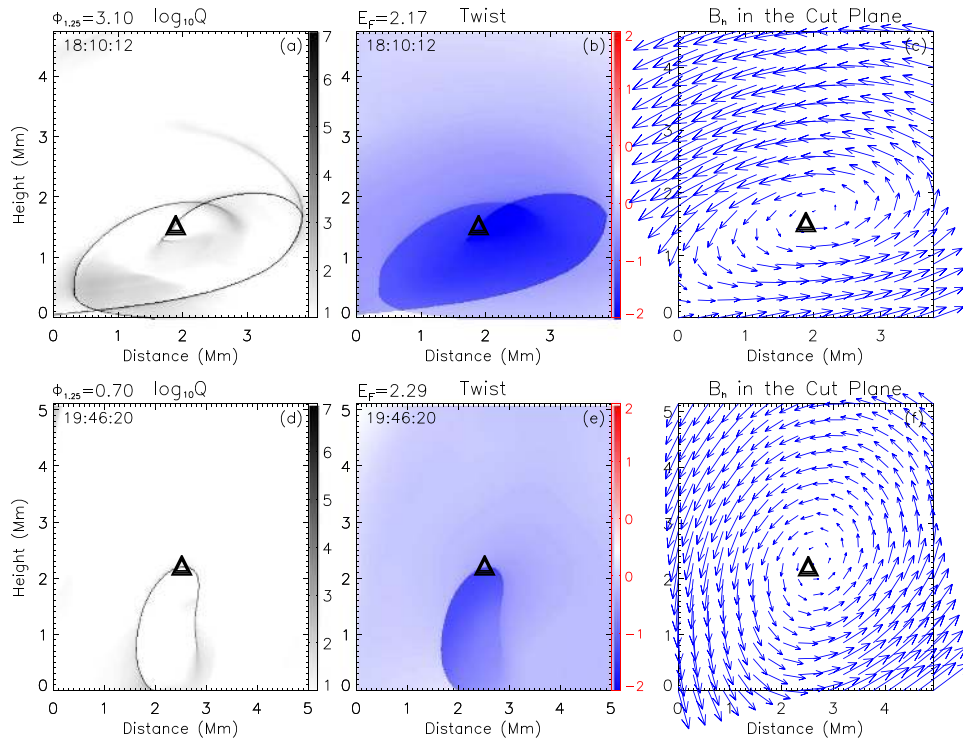


Figure 13. Magnetic features in the vertical cuts, perpendicular to the flux rope at PIL1 in AR 11158, at Time2 (post-CME1 but pre-CME2) and Time3 (post-CME2). Same layout as panels (a)–(f) in Figure 8. $\Phi_{1,25}$, given at the headers of panels (a) and (d), are vertical magnetic flux (in units of 10^{19} Mx) from the strong T_w region ($|T_w| \gtrsim 1.25$) at each time, respectively. E_F , given at the header of panels (b) and (e), are magnetic free energy (in units of 10^{32} erg) at the two times.

eruption of the flux rope along PIL1 resulted in the reconnection of the upper two flux ropes along PIL2 remain unclear, though the observation data have been analyzed. The first CME can remove the common overlying arcades, cause disturbance, compress the fields in the neighbor system, and even reconnect with neighbor fields. Somehow the equilibrium of the triple-decker flux rope is broken, and the upper two flux ropes reconnect. The key reason for the D-type eruption studied here is that the two flux rope systems are close enough that CME1 can impact on the pre-eruptive structure of CME2. It should be noted that the triple-decker flux rope presented here delivers a quite uncommon configuration, of which equilibrium and evolution are worth studying in the future.

A well-studied D-type QH CME from AR 11402, with a waiting time of 48 minutes, also suggests that the CME was initiated by its predecessor (Cheng et al. 2013). The first CME may have opened some overlying arcade, allowed the neighboring fields to expand, and lowered the downward magnetic tension above the neighboring flux rope, leading to the second CME. The scenario, that one eruption weakens the magnetic confinement of another flux tube system and promotes other eruptions, has been demonstrated in simulations (e.g., Török et al. 2011; Lynch & Edmondson 2013). The configuration in Török et al. (2011) contains a pseudo-streamer (PS), with two flux ropes located in the PS and one flux rope located next to the PS. The flux rope outside expands and erupts as the first CME, causing a breakout reconnection above one of the flux ropes in the PS, resulting in the second CME; the current sheet formed below the second erupted flux rope causes reconnection at the overlying arcades of the other flux rope in the PS, leading to the third CME. The latter two CMEs can happen in a more generic configuration, without a flux rope outside the PS to erupt at first to trigger them, although the

Table 1
Force-free and Divergence-free Parameters

Time	θ (deg)	$\langle f_i \rangle (\times 10^{-3})$
2011-02-14T17:10:12	6.70	2.08
2011-02-14T18:10:12	7.19	2.11
2011-02-14T19:46:20	6.97	1.90
2012-03-06T23:46:14	5.82	2.91
2012-03-07T00:58:14	6.78	2.78
2012-03-07T01:10:14	6.02	2.70

underlying evolution is the same (Lynch & Edmondson 2013). The model of Török et al. (2011) or Lynch & Edmondson (2013) is applicable in a PS configuration. More generally, it is applicable in a configuration with a closed flux system containing a flux rope located near the erupting flux rope, e.g., a quadrupolar configuration, such as the D-type CME and its preceding one from AR 10030 shown in Figure 4. The CME had a waiting time of 1 hr, following a process similar to the second and third CMEs in Török et al. (2011), or the two CMEs in Lynch & Edmondson (2013), according to Gary & Moore (2004): the core flux rope of the first CME was released from one flux tube system in a quadrupolar region by a breakout reconnection at the X point above the region; the neighboring flux rope started to expand and finally erupted out owing to the decrease of the overlying magnetic tension, which was caused by the reconnection at the current sheet formed below the first erupted flux rope.

More generally, in an AR with multiple flux tube systems, one eruption causing destabilizations that promote other eruptions could be described as a “domino effect” scenario (Liu et al. 2009; Zuccarello et al. 2009). The peak value of the waiting time distribution of the D-type QH CMEs, around

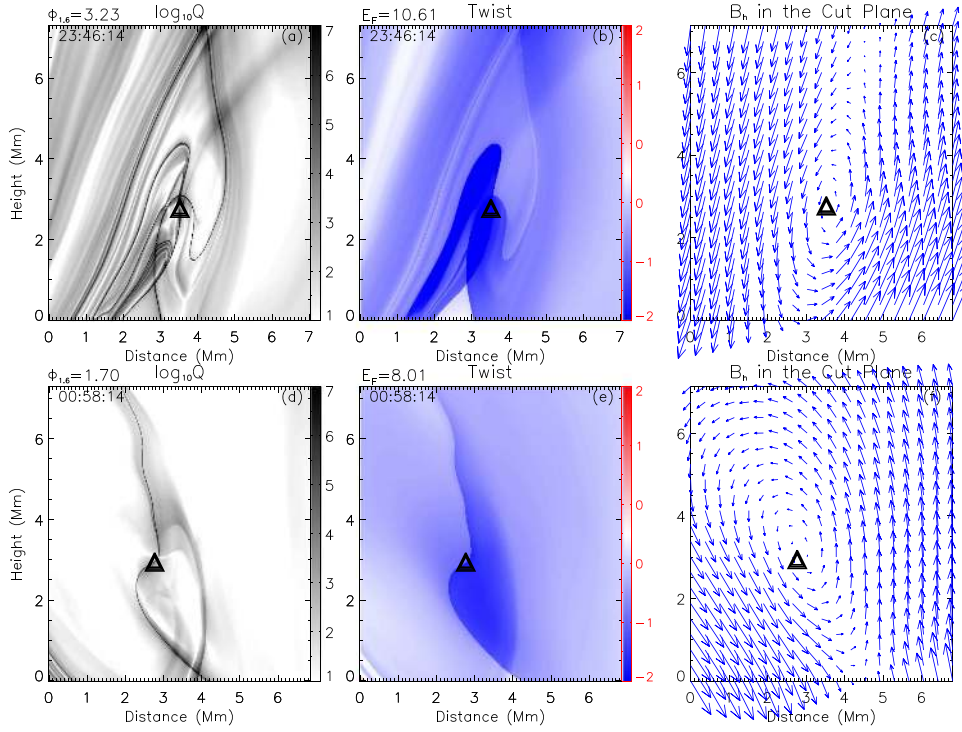


Figure 14. Magnetic features in the vertical cuts, perpendicular to the flux rope at PIL1 in AR 11429, at Time1 (pre-CME1) and Time2 (post-CME1 but pre-CME2). Same layout as in Figure 13.

1.5 hr, could be the characteristic timescale of the growth of destabilization caused by their predecessors. These kinds of consecutive CMEs with extremely short waiting times are sometimes called “twin-CMEs” or “sympathetic-CMEs,” although they are not necessarily produced from the same AR (e.g., Balasubramaniam et al. 2011; Schrijver & Title 2011; Yang et al. 2012; Ding et al. 2013, 2014; Shen et al. 2013). The source locations of a D-type QH CME and its predecessor are expected to be located close to each other, or have some magnetic connection in which one eruption can induce the other one.

Note that there is another slightly lower peak around 9.5 hr in the waiting time distribution of D types, which may be due to the method of classification, or even a different mechanism from the one for those with a waiting time around 1.5 hr.

In conclusion, through the two cases studied in depth, we propose possible mechanisms for most of the two types of QH CMEs, i.e., the ones located around the peak of the waiting time distribution: an S-type QH CME can occur in a recurring energy release process by free energy regain, while a D-type QH CME can happen when disturbed by its preceding one. The different peak values of the waiting time distributions, 7.5 hr for S-type and 1.5 hr for D-type QH CMEs, might be the characteristic timescales of the two different scenarios. The classification is only based on the source PILs. An S-type QH CME may also happen when disturbed by its predecessor, following a process similar to that for the D-type QH CME, for example, in a configuration with more than one flux rope vertically located above the same PIL, like the ones in AR 11429, in which change (reconnection, expulsion, etc.) of the upper flux ropes caused the eruption of the lower one. More cases with high spatial and temporal resolution data (e.g., data from *SDO*) are worth studying to discover more scenarios.

We thank our anonymous referee for his/her constructive comments that significantly improved the manuscript. We acknowledge the use of the data from HMI and AIA instruments on board *Solar Dynamics Observatory (SDO)*; EIT, MDI, and LASCO instruments on board *Solar and Heliospheric Observatory (SOHO)*; and *Transition Region and Coronal Explorer (TRACE)*. This work is supported by the grants from NSFC (41574165, 41421063, 41274173, 41474151, 41131065), CAS (Key Research Program KZZD-EW-01-4), MOEC (20113402110001), and the fundamental research funds for the central universities.

Appendix A Quality of NLFF Extrapolation

Lorentz force ($\mathbf{J} \times \mathbf{B}$, where \mathbf{J} is the current density) and the divergence of the magnetic field ($\nabla \cdot \mathbf{B}$) should be as small as possible to meet force-free and divergence-free conditions in the NLFF coronal fields. We follow Liu et al. (2016b) and Wheatland et al. (2000), using two parameters, θ (the angle between \mathbf{B} and \mathbf{J}) and $\langle |f_i| \rangle$ (fractional flux increase), to measure the quality of the model fields:

$$\sigma_J = \left(\sum_{i=1}^n \frac{|\mathbf{J} \times \mathbf{B}_i|}{B_i} \right) / \sum_{i=1}^n J_i$$

$$\theta = \sin^{-1} \sigma_J, \quad (5)$$

$$\langle |f_i| \rangle = \frac{1}{n} \sum_{i=1}^n \frac{|\nabla \cdot \mathbf{B}_i| \Delta V_i}{B_i \cdot \Delta S_i}, \quad (6)$$

where n is the number of the grid points and ΔV_i and ΔS_i are the volume and surface area of the i th cell, respectively. σ_J gives the average $\sin \theta$ weighted by J . See Table 1 for θ and $\langle |f_i| \rangle$ in the aforementioned (and also mentioned in the next three

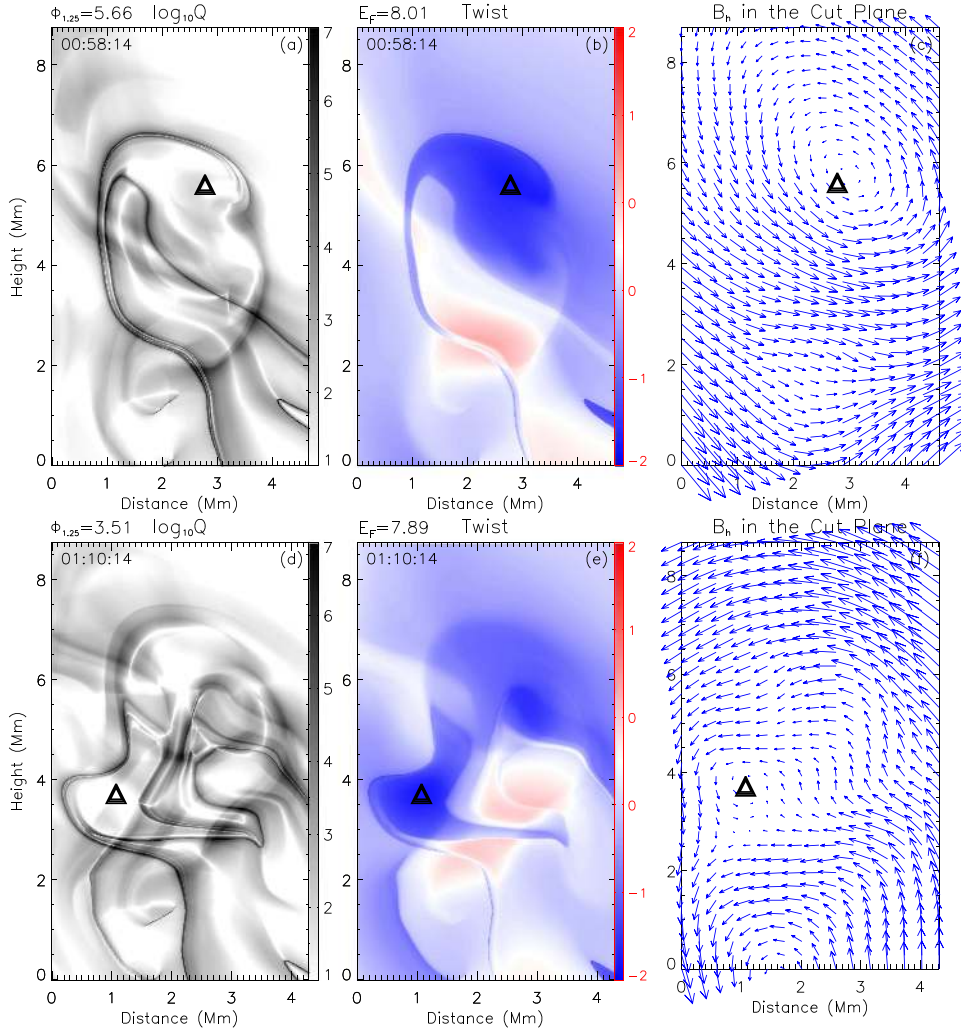


Figure 15. Magnetic features in the vertical cuts, perpendicular to the flux rope at PIL2 in AR 11429, at Time2 (post-CME1 but pre-CME2) and Time3 (post-CME2). Same layout as in Figure 13.

sections) model NLFF fields, which all meet force-free and divergence-free conditions.

Appendix B Change of Magnetic Parameters during CME2 in AR 11158

In Section 3.2, the magnetic parameters at the source location (L1) are studied in pre-CME1 (at Time1) and post-CME1 but pre-CME2 (at Time2) corona. In this appendix, we perform a similar analysis in a plane perpendicular to the flux rope axis along PIL1 in the post-CME2 corona (2011-02-14T19:46:20 UT, defined as Time3), as shown in Figures 13(d), (e), and (f) (Q , T_w , and B_{\parallel} , respectively). The parameters at Time2 are shown in Figures 13(a)–(c) for comparison. The triangles mark the peak T_w position, i.e., the position where the flux rope axis threads the plane. At Time3, the pronounced Q boundary, strong T_w region, and rotational structure around the peak T_w point in the in-plane vector fields evidence a flux rope. However, the vertical magnetic flux from the strong T_w region ($|T_w| \gtrsim 1.25$) calculated by Equation (3) is reduced by 77% after CME2 (from 3.10×10^{19} Mx at Time2 to 0.70×10^{19} Mx at Time3, shown at the header of Figures 13(a) and (d)). The magnetic free energy still shows

a slight increase of 5.5% (from 2.17×10^{32} erg at Time2 to 2.29×10^{32} erg at Time3, as shown at the header of Figures 13(b) and (e)), which is below the uncertainty. CME2 being confirmed to be correlated to the source location based on observation and the decrease of twist of the rope both evidence that the flux rope is involved in the eruption. However, this information is not enough for distinguishing whether the flux rope at Time3 is a remnant of the previous flux rope, which may undergo a partial eruption accompanied by topology reconfiguration during CME2, or is a newly emerged/reformed one after CME2. Study of the CME2's eruption detail is beyond this paper's scope.

Appendix C Change of Magnetic Parameters during CME1 in AR 11429

In Section 3.3, the magnetic parameters at the source location of CME2 (L2) are studied in pre-CME1 (at Time1) and post-CME1 but pre-CME2 (at Time2) corona to see the possible influence from CME1 to CME2. In this section, we perform a similar analysis at the source location of CME1 (L1) to see what happened during CME1. Q , T_w , and B_{\parallel} are calculated in a plane perpendicular to the flux rope axis along PIL1 at Time1



(Figures 14(a)–(c)) and Time2 (Figures 14(d)–(f)), respectively. Flux rope is found at PIL1 both before CME1 and after CME1. The vertical magnetic flux from the strong T_w region, with a threshold of 1.25 turns ($|T_w| \gtrsim 1.25$), shows no significant change. However, when changing the threshold to 1.6 turns ($|T_w| \gtrsim 1.6$), the vertical magnetic flux shows a significant reduction of 47% (from 3.23×10^{19} Mx at Time1 to 1.70×10^{19} Mx at Time2, shown at the header of Figures 14(a) and (c)). CME1 has been confirmed to be related to the source location L1 based on observation, as discussed in Section 2.3; thus, the flux rope should be responsible for the eruption. Its representative axial flux with $|T_w| \gtrsim 1.6$ decreased, at the mean time, while the flux with $|T_w| \gtrsim 1.25$ almost remained constant. Partial expulsion of the flux rope, accompanied by replenishment of twist through shear motion or reconnection, can explain the phenomenon.

Appendix D

Change of Magnetic Parameters during CME2 in AR 11429

In this appendix, we perform a similar analysis to that in Section 3.3 in a plane perpendicular to the flux rope axis along PIL2 in the post-CME2 corona (2012-03-07T01:10:12 UT, defined as Time3), as shown in Figures 15(d), (e), and (f) (Q , T_w , and $B_{||}$, respectively), to see the eruption detail during CME2. The parameters at Time2 are shown in Figures 15(a)–(c) for comparison. After CME2, there still existed a flux rope along PIL2, showing a significant topology change compared to that at Time2. The vertical magnetic flux from the strong T_w region ($|T_w| \gtrsim 1.25$) calculated by Equation (3) decreased by 38% after CME2 (from 5.66×10^{19} Mx at Time2 to 3.51×10^{19} Mx at Time3, shown at the header of Figures 15(a) and (d)). The magnetic free energy also shows a slight decrease of 1.5% (from 8.01×10^{32} erg at Time2 to 7.89×10^{32} erg at Time3, as shown at the header of Figures 15(b) and (e)), which is far below the uncertainty. The flux ropes traced by the model method in our cases and two eruptive events in Liu et al. (2016b) all show a twist remnant after the eruption. We come up with two possible explanations: it is due to a partial expulsion process or quick replenishment of twist through emergence/reformation after the eruption. The phenomenon is worth studying in the future.

ORCID

Yuming Wang  <https://orcid.org/0000-0002-8887-3919>
 Rui Liu  <https://orcid.org/0000-0003-4618-4979>
 M. Temmer  <https://orcid.org/0000-0003-4867-7558>
 J. K. Thalmann  <https://orcid.org/0000-0001-8985-2549>
 Jiajia Liu  <https://orcid.org/0000-0003-2569-1840>
 Kai Liu  <https://orcid.org/0000-0003-2573-1531>
 Quanhao Zhang  <https://orcid.org/0000-0003-0565-3206>
 A. M. Veronig  <https://orcid.org/0000-0003-2073-002X>

References

- Akiyama, S., Yashiro, S., & Gopalswamy, N. 2007, *AdSpR*, 39, 1467
 Amari, T., Luciani, J. F., Mikic, Z., & Linker, J. 1999, *ApJL*, 518, L57
 Balasubramaniam, K. S., Pevtsov, A. A., Cliver, E. W., Martin, S. F., & Panasenco, O. 2011, *ApJ*, 743, 202
 Berger, M. A., & Prior, C. 2006, *JPhA*, 39, 8321
 Brueckner, G. E., Howard, R. a., Koomen, M. J., et al. 1995, *SoPh*, 162, 357
 Chatterjee, P., & Fan, Y. 2013, *ApJL*, 778, L8
 Chen, C., Wang, Y., Shen, C., et al. 2011, *JGR*, 116, A12108
 Cheng, X., Zhang, J., Ding, M. D., et al. 2013, *ApJL*, 769, L25
 Chertok, I. M., Grechnev, V. V., Hudson, H. S., & Nitta, N. V. 2004, *JGR*, 109, 1
 Chintzoglou, G., Patsourakos, S., & Vourlidas, A. 2015, *ApJ*, 809, 34
 DeVore, C. R., & Antiochos, S. K. 2008, *ApJ*, 680, 740
 Ding, L., Jiang, Y., Zhao, L., & Li, G. 2013, *ApJ*, 763, 30
 Ding, L., Li, G., Dong, L.-H., et al. 2014, *JGR*, 119, 1463
 Filippov, B. 2013, *ApJ*, 773, 10
 Gary, G. A., & Moore, R. L. 2004, *ApJ*, 611, 545
 Gibson, S. E., & Fan, Y. 2006, *ApJL*, 637, L65
 Handy, B., Acton, L., Kankelborg, C., et al. 1999, *SoPh*, 187, 229
 Hoeksema, J. T., Liu, Y., Hayashi, K., et al. 2014, *SoPh*, 289, 3483
 Hood, A. W., & Priest, E. R. 1981, *GApFD*, 17, 297
 Jing, J., Tan, C., Yuan, Y., et al. 2010, *ApJ*, 713, 440
 Kaiser, M. L., Kucera, T. a., Davila, J. M., et al. 2008, *SSRv*, 136, 5
 Kienreich, I. W., Veronig, A. M., Muhr, N., et al. 2011, *ApJL*, 727, L43
 Kliem, B., & Török, T. 2006, *PhRvL*, 96, 255002
 Kliem, B., Török, T., Titov, V. S., et al. 2014, *ApJ*, 792, 107
 Lemen, J. R., Title, A. M., Akin, D. J., et al. 2012, *SoPh*, 275, 17
 Li, T., & Zhang, J. 2013, *ApJL*, 778, L29
 Liu, C., Lee, J., Karlický, M., et al. 2009, *ApJ*, 703, 757
 Liu, L., Wang, Y., Wang, J., et al. 2016a, *ApJ*, 826, 119
 Liu, R., Kliem, B., Titov, V. S., et al. 2016b, *ApJ*, 818, 148
 Liu, R., Kliem, B., Török, T., et al. 2012, *ApJ*, 756, 59
 Liu, Y. 2008, *ApJL*, 679, L151
 Lynch, B. J., & Edmondson, J. K. 2013, *ApJ*, 764, 87
 MacTaggart, D., & Hood, A. W. 2009, *A&A*, 508, 445
 Moon, Y.-J., Chae, J., Wang, H., & Park, Y. 2003a, *AdSpR*, 32, 1953
 Moon, Y.-J., Choe, G. S., Wang, H., & Park, Y. D. 2003b, *ApJ*, 588, 1176
 Nitta, N. V., & Hudson, H. S. 2001, *GeoRL*, 28, 3801
 Pesnell, W. D., Thompson, B. J., & Chamberlin, P. C. 2012, *SoPh*, 275, 3
 Schmieder, B. 2006, *JApA*, 27, 139
 Schou, J., Scherrer, P. H., Bush, R. I., et al. 2012, *SoPh*, 275, 229
 Schrijver, C. J. 2009, *AdSpR*, 43, 739
 Schrijver, C. J., & Title, A. M. 2011, *JGR*, 116, A04108
 Shen, C., Li, G., Kong, X., et al. 2013, *ApJ*, 763, 114
 Soenen, A., Zuccarello, F. P., Jacobs, C., et al. 2009, *A&A*, 501, 1123
 Su, J. T., Jing, J., Wang, S., Wiegelmann, T., & Wang, H. M. 2014, *ApJ*, 788, 150
 Su, Y., van Ballegoijen, A., McCauley, P., et al. 2015, *ApJ*, 807, 144
 Subramanian, P., & Dere, K. P. 2001, *ApJ*, 561, 372
 Sun, X., Bobra, M. G., Hoeksema, J. T., et al. 2015, *ApJL*, 804, L28
 Sun, X., Hoeksema, J. T., Liu, Y., Chen, Q., & Hayashi, K. 2012, *ApJ*, 757, 149
 Thalmann, J. K., Su, Y., Temmer, M., & Veronig, A. M. 2015, *ApJL*, 801, L23
 Thalmann, J. K., Wiegelmann, T., & Raouafi, N.-E. 2008, *A&A*, 488, L71
 Tian, L., Liu, Y., & Wang, J. 2002, *SoPh*, 209, 361
 Titov, V. S. 2007, *ApJ*, 660, 863
 Titov, V. S., & Démoulin, P. 1999, *A&A*, 351, 707
 Titov, V. S., Hornig, G., & Démoulin, P. 2002, *JGR*, 107, 1164
 Titov, V. S., Priest, E. R., & Démoulin, P. 1993, *A&A*, 276, 564
 Török, T., & Kliem, B. 2003, *A&A*, 406, 1043
 Török, T., & Kliem, B. 2005, *ApJL*, 630, L97
 Török, T., Panasenco, O., Titov, V. S., et al. 2011, *ApJL*, 739, L63
 Wang, Y., Chen, C., Gui, B., et al. 2011, *JGR*, 116, A04104
 Wang, Y., Liu, L., Shen, C., et al. 2013, *ApJL*, 763, L43
 Wang, Y., & Zhang, J. 2007, *ApJ*, 665, 1428
 Webb, D. F., & Howard, T. A. 2012, *LRSF*, 9, 3
 Wheatland, M. S., Sturrock, P. a., & Roumeliotis, G. 2000, *ApJ*, 540, 1150
 Wiegelmann, T. 2004, *SoPh*, 219, 87
 Wiegelmann, T., Thalmann, J. K., Inhester, B., et al. 2012, *SoPh*, 281, 37
 Yang, J., Jiang, Y., Zheng, R., et al. 2012, *ApJ*, 745, 9
 Yashiro, S. 2004, *JGR*, 109, A07105
 Yashiro, S., Michalek, G., Akiyama, S., Gopalswamy, N., & Howard, R. A. 2008, *ApJ*, 673, 1174
 Zhang, J., & Wang, J. 2002, *ApJL*, 566, L117
 Zhou, G., Wang, J., & Cao, Z. 2003, *A&A*, 397, 1057
 Zuccarello, F., Romano, P., Farnik, F., et al. 2009, *A&A*, 493, 629
 Zuccarello, F. P., Aulanier, G., & Gilchrist, S. A. 2016, *ApJL*, 821, L23